

Banner appropriate to article type will appear here in typeset article

Structure of an axisymmetric turbulent boundary layer under adverse pressure gradient: a large-eddy simulation study

Di Zhou^{1,2}, Kan Wang^{1,3} and Meng Wang^{1†}

¹Department of Aerospace and Mechanical Engineering, Institute for Flow Physics and Control, University of Notre Dame, Notre Dame, IN 46556, USA

²Present address: Graduate Aerospace Laboratories, California Institute of Technology, Pasadena, CA 91125, USA

³Present address: Cadence Design Systems Inc., San Jose, CA 95134, USA

(Received xx; revised xx; accepted xx)

The spatial characteristics and structure of an axisymmetric turbulent boundary layer under strong adverse pressure gradient and weak transverse curvature are investigated using incompressible large-eddy simulation. The boundary layer is on a 20° tail cone of a body of revolution at a length-based Reynolds number of 1.9×10^6 . The simulation results are in agreement with the experimental measurements of Balantrapu *et al.* (*J. Fluid Mech.*, vol. 929, 2021) and significantly expand the experimental results with new flow-field details and physical insights. The mean streamwise velocity profiles exhibit a shortened logarithmic region and a longer wake region compared with planar boundary layers at zero pressure gradient. With the embedded-shear-layer scaling, self-similarity is observed for the mean velocity and all three components of turbulence intensity. The azimuthal-wavenumber spectra of streamwise velocity fluctuations possess two peaks in the wall-normal direction, an inner peak at the wavelength of approximately 100 wall units and an outer peak in the wake region with growing strength, wavelength and distance to the wall in the downstream direction. Two-point correlations of streamwise velocity fluctuations show significant downstream growth and elongation of turbulence structures with increasing inclination angle. However, relative to the boundary-layer thickness, the correlation structures decrease in size in the downstream direction. The distributions of streamwise and wall-normal integral lengths across the boundary-layer thickness resemble those of zero-pressure-gradient planar boundary layers, whereas the azimuthal integral length deviates from the planar boundary-layer behavior at downstream stations.

1. Introduction

Turbulent boundary layers (TBLs) are among the most extensively studied topics in fluid dynamics. In recent decades, a wealth of experimental and numerical simulation data has been amassed over a broad range of Reynolds numbers and flow conditions. Analysis of the data has led to significant advancements in understanding of TBLs, as highlighted in

† Email address for correspondence: m.wang@nd.edu

the recent reviews of Marusic *et al.* (2010), Smits *et al.* (2011) and Jiménez (2018). Despite these advancements, knowledge of TBLs developing under adverse pressure gradient (APG) conditions remains less mature compared to that of canonical zero-pressure-gradient (ZPG) TBLs. This knowledge gap presents ongoing challenges to the accurate prediction and control of such flows, which are prevalent in engineering applications. The presence of APG can alter the TBL behavior significantly, potentially leading to flow separation and associated detrimental effects. An enhanced understanding of the flow physics and structures in these conditions is therefore vital to the design and optimization of engineering flow systems, and forms the foundation for developing effective flow-control strategies.

APG TBLs have been studied actively since the 1950s. Earlier investigations, such as those by Clauser (1954) and Coles (1956), were predominantly experimental and analytical, and limited to narrow ranges of flow conditions due to the constraints of experimental techniques at the time. The advancement in sensors and measurement technology since the late 1960s facilitated more detailed flow field measurements, and by the 1990s, high-fidelity numerical simulations were introduced as a powerful new tool to the study. It is now generally understood that (e.g., Spalart & Watmuff (1993); Marusic & Perry (1995); Aubertine & Eaton (2005); Monty *et al.* (2011)), under the influence of APG, the mean-velocity profile develops a larger wake region, and the log-region profile shifts below the classical log-law profile for ZPG TBLs. Additionally, the turbulent kinetic energy decreases near the wall while a dominant secondary peak develops in the outer layer. Beyond low-order turbulence statistics, APG also has a significant impact on turbulence structures (Krogstad & Skåre 1995; Lee & Sung 2009; Harun *et al.* 2013; Maciel *et al.* 2017; Lee 2017; Volino 2020; Gungor *et al.* 2024). Near-wall streaks are weakened and become wider, large-scale turbulent motions in the outer region are energized, and streamwise correlations are decreased with increased inclination angles of coherent structures. Multiple scaling parameters have been proposed for APG TBLs (Zagarola & Smits 1998; Aubertine & Eaton 2006; Schatzman & Thomas 2017; Maciel *et al.* 2018; Wei & Knopp 2023; Chen *et al.* 2023). In particular, Schatzman & Thomas (2017) experimentally investigated the TBL on a two-dimensional (2-D) ramp with steady and unsteady APG imposed by an airfoil from above with plasma actuation, and proposed an embedded-shear-layer scaling in terms of the shear-layer vorticity thickness and the velocity defect at the upper inflection point of the mean streamwise velocity profile. Using this scaling, similarity was observed in both space and time for the measured mean and phase-averaged velocity profiles and, to a lesser degree, the phase-averaged streamwise turbulence intensity and Reynolds shear stress. Schatzman & Thomas (2017) also tested the embedded-shear-layer scaling with some previously published APG TBL measurements, and confirmed its general applicability.

Most of the previous APG TBL studies were focused on plane-wall or 2-D ramp geometries. When flow encounters an axisymmetric body of revolution (BOR) in the axial direction, an axisymmetric TBL forms in the presence of streamwise pressure gradients. This configuration is common in various aerodynamic and hydrodynamic engineering applications, such as aircraft fuselages and submarine hulls, and has thus motivated many investigations as well. Patel *et al.* (1974) performed detailed measurements of a thick axisymmetric TBL in the tail region of a BOR, revealing different behavior compared to thin planar TBLs, such as significant static pressure variations across the boundary layer and decreasing turbulence levels toward downstream. Hammache *et al.* (2002) conducted particle-image-velocimetry (PIV) measurements over an axisymmetric Stratford ramp (Stratford 1959) constituting the tail section of a BOR. Under streamwise APG, the TBL is continuously on the verge of separation and thickens rapidly. The outer-scaled mean streamwise velocity profiles exhibited a pronounced wake region and self-similarity. A widely studied BOR in recent years is the DARPA SUBOFF geometry (Groves *et al.* 1989; Huang *et al.* 1992) with or without

appendages. Posa & Balaras (2016, 2020) conducted large-eddy simulation (LES) of flow over a fully appended SUBOFF to examine the effects of appendages and their junction flows on the development of the downstream boundary layer and wake, and their Reynolds number dependence. The surface geometry was treated using an immersed-boundary method, and good agreement with experimental data was demonstrated. Kumar & Mahesh (2018) performed LES of flow over the SUBOFF hull without appendages at a reduced Reynolds number and zero angle of attack, and also obtained agreement with higher-Reynolds-number experimental results. Their axisymmetric TBL on the cylindrical midsection of the hull exhibited higher skin friction and more pronounced radial decay of turbulence compared with a ZPG planar TBL. Additionally, the axisymmetric wake showed self-similarity in mean streamwise velocity but not in turbulence intensities. Note that the aforementioned LES studies are primarily focused on the behavior of turbulence statistics in the boundary layer and the wake, with little attention to the turbulence structures in the boundary layer and the pressure gradient effect.

In a recent experimental study, Balantrapu *et al.* (2021, 2023) at Virginia Tech (VT) focused on a thick axisymmetric TBL that develops on the tail cone of a BOR at zero angle of attack. The BOR features a cylindrical centerbody of diameter $D = 0.432$ m and equal length, an ellipsoidal nose also of length D , and a tail cone of length $1.17D$ with a 20° half apex angle. Measurements were conducted with a free-stream velocity of 22 m/s, corresponding to a Reynolds number of 1.9×10^6 based on the BOR length. Hotwire velocity measurements were supplemented by non-time-resolved PIV measurements in a smaller region, and surface pressure fluctuations were measured using a longitudinal array of microphones. Their single hotwire measurements revealed self-similarity for the streamwise mean-velocity and turbulence intensity profiles when analyzed using the embedded-shear-layer scaling of Schatzman & Thomas (2017). Through frequency-spectral analysis of the fluctuating streamwise velocity, they observed that, as in planar TBLs, large-scale motions were energized and grew roughly in proportion to the boundary-layer thickness. By comparing the two-point streamwise velocity correlations estimated from single-point hotwire data and Taylor's hypothesis with those from PIV measurements, it was noted that the convection velocity was significantly larger than the local mean velocity. All analyses were based on outer scales because of limited near-wall access in the measurements.

The present numerical study was started in parallel with the VT experiment of Balantrapu *et al.* (2021, 2023), with the objectives of assisting the design of the BOR, particularly in the choice of the tail-cone apex angle that produces a thick boundary layer without separation, cross-validating the experiment and computational results, and obtaining more comprehensive spatial and temporal details of the flow and thereby new insight into the evolution of the axisymmetric TBL under strong APG. Accurate prediction of the tail-cone TBL also served as a precursor for a related study of the noise from a rotor ingesting the TBL at the tail-cone end (Zhou *et al.* 2024). Given the high Reynolds number and the expansive surface area of the BOR, conducting LES posed significant computational challenges, and a side goal was therefore to explore means to mitigate the computational cost while providing a highly accurate description of the TBL in the tail-cone region. To this end, a wall model was employed in the LES in the nose and centerbody sections of the BOR, but the crucial tail-cone section was wall-resolved. This approach, discussed in more detail in §2.1, was validated by comparing its results with the results of fully wall-resolved LES (Zhou *et al.* 2020). Using the simulation data, a detailed analysis of the tail-cone TBL has been carried out to gain a better understanding of how APG and transverse curvature influence the evolution of the TBL statistical properties and structure. The results are presented in this paper. In addition to new understanding and insights, the simulation results complement the

experimental data of Balantrapu *et al.* (2021, 2023) for this fundamentally interesting flow with significantly expanded flow regions and details.

The remainder of the paper is structured as follows: Section 2 describes the numerical approach, flow configuration, and simulation set-up including grids and boundary conditions. In §3, the simulation results are validated through grid refinement and comparison with the experimental data of Balantrapu *et al.* (2021, 2023) in terms of velocity and surface-pressure statistics, spectra and correlations. Section 4 is dedicated to a detailed analysis of the turbulence statistics and structures of the tail-cone TBL and their evolution under the APG. Quantities examined include the velocity statistics profiles and their scaling, pre-multiplied energy spectra, two-point correlation structures and their inclination angles, and integral length scales. Finally, the key findings of the study are summarized in §5.

2. Computational methodology

2.1. Numerical approach

Flow simulations are conducted using a finite-volume, unstructured-mesh LES code developed at Stanford University (You *et al.* 2008). The spatially-filtered, incompressible Navier-Stokes equations are solved with second-order accuracy using cell-based, low-dissipative and energy-conservative spatial discretization and a fully implicit, fractional-step time-advancement method with the Crank–Nicolson scheme. The Poisson equation for pressure is solved using the method of Generalized Product Bi-Conjugate Gradient with safety convergence (GPBiCGSafe) proposed by Fujino & Sekimoto (2012). The subgrid-scale stress is modeled using the dynamic Smagorinsky model (Germano *et al.* 1991; Lilly 1992).

Because of the large surface area of the BOR and high Reynolds number, LES of the flow is computationally very expensive if it resolves all the energetic eddies down to the wall. In order to reduce the computational cost, a zonal wall-modeled LES (WMLES) approach is used, where a wall model is applied to the nose and centerbody sections, whereas in the downstream tail-cone section, which is of primary interest, the LES is wall-resolved. In the sections with WMLES, the equilibrium stress-balance wall model (Cabot & Moin 2000; Wang & Moin 2002) is employed to account for the effect of the near-wall dynamic eddies in terms of approximate wall shear-stress boundary conditions provided to the LES. The accuracy of this approach has been validated previously (Zhou *et al.* 2020) by comparing the results of the zonal WMLES with those from a wall-resolved LES (WRLES) for the entire BOR. In particular, the comparison demonstrates that the tail-cone TBL is relatively insensitive to the detailed near-wall turbulence structures in the upstream boundary layer that are present in the WRLES but unresolved in the WMLES, possibly due to the strong perturbation to the flow produced by the sharp corner of the junction between the centerbody and the tail cone. A similar zonal WMLES approach was used by Posa & Balaras (2020) in their LES of flow over the SUBOFF geometry using an immersed boundary method, also with satisfactory results for the tail-cone TBL in comparison with experimental data at equivalent Reynolds numbers.

2.2. Configuration and simulation set-up

The physical conditions for the present simulations are consistent with those in the experiment of Balantrapu *et al.* (2021). The flow configuration and boundary conditions are shown schematically in figure 1. As mentioned earlier, the BOR consists of a cylindrical section in the middle, a 2:1 ellipsoidal nose, and a tail cone that connects to the centerbody at one end and a cylindrical support pole at the other end. For convenience, the diameter D of the centerbody is used as the length scale for normalization. The nose and the centerbody both

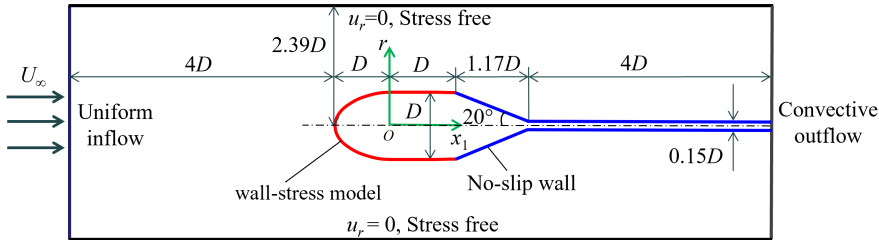


Figure 1: Simulation set-up for flow over a body of revolution.

have a length equal to D , the tail cone has a length of $1.17D$ with a 20° half apex angle, and the support pole has a diameter of $0.15D$. A circumferential trip ring with a rectangular cross-section of $0.002D \times 0.001D$ is placed at the downstream end of the nose to induce transition in the boundary layer. The height of the trip ring is one half of the experimental value, which is found to produce a closer match with the experimental boundary-layer thickness in the downstream. Note that the flow-details around the trip is not well-resolved. The BOR is at zero angle of attack, and the Reynolds number is $Re_L = U_\infty L / \nu = 1.9 \times 10^6$ based on the free-stream velocity U_∞ and the total length of the BOR, $L = 3.17D$.

Simulations are conducted in a cylindrical domain of length $11.2D$ and radius $2.39D$. The radius of the domain is chosen to provide the same blockage ratio as in the VT wind tunnel. The center of the cross-section at the nose end, chosen as the origin of the coordinates, is $5D$ downstream from the inlet. For convenience, both a Cartesian coordinate system (x_1 - x_2 - x_3) with velocity components (u_1 , u_2 , u_3) and a cylindrical coordinate system (x_1 - r - θ) with velocities (u_1 , u_r , u_θ) are used simultaneously in this paper, where the x_3 - and θ -coordinates obeying the right-hand rule. The boundary conditions consist of a uniform inflow at the inlet, stress-free conditions with radial velocity $u_r = 0$ on the outer boundary, approximate wall-shear stress for WMLES and no-slip condition for WRLES on the respective solid surfaces, and convective outflow conditions at the exit.

The computational mesh consists of structured-mesh blocks around the surfaces of the BOR and the support pole and unstructured-mesh blocks in the outer region. Over the wall-modeled centerbody, the meshes are relatively coarse with 380 streamwise cells and 1472 azimuthal cells. In the middle of the centerbody, the grid spacings in wall units are $\Delta x^+ \approx 130$, $\Delta r_{\min}^+ \approx 25$ and $(R\Delta\theta)^+ \approx 68$, where R is the centerbody radius, and there are 25 mesh cells across the boundary-layer thickness. Since the tail-cone section is the focus of the investigation, it is wall-resolved, and the mesh is significantly finer in wall units. The transition to the wall-resolved mesh is gradual and starts at $0.2D$ upstream of the centerbody-tail cone junction. To check grid convergence, simulations are performed on two meshes with different resolutions in the tail-cone section. On the coarse mesh, the tail-cone section has 800 streamwise cells, 1472 uniformly spaced azimuthal cells (same as on the centerbody), and 90 cells across the thickness of the TBL at the end of the cone. Except in the immediate neighborhood of the sharp centerbody-tail cone corner, the streamwise and azimuthal grid spacings are less than 30 and 60 wall units, respectively, and decrease to 12 and 2 at the end of the tail cone. The wall-normal spacing for the first off-wall cell is less than 2 wall units and decreases to 0.8 at the tail-cone end. On the fine mesh, the tail-cone section has 1200 and 2944 uniformly spaced cells in the streamwise and azimuthal directions, respectively, and 170 cells across the thickness of the TBL at the tail-cone end. The streamwise and azimuthal grid spacings in wall units are both less than 30 slightly ($0.05D$) downstream of the upper tail-cone corner, and decrease to 6 and 1, respectively, at the tail-cone end. The wall-normal spacing for the first off-wall cell on the tail cone decreases from 1.2 to 0.3 along

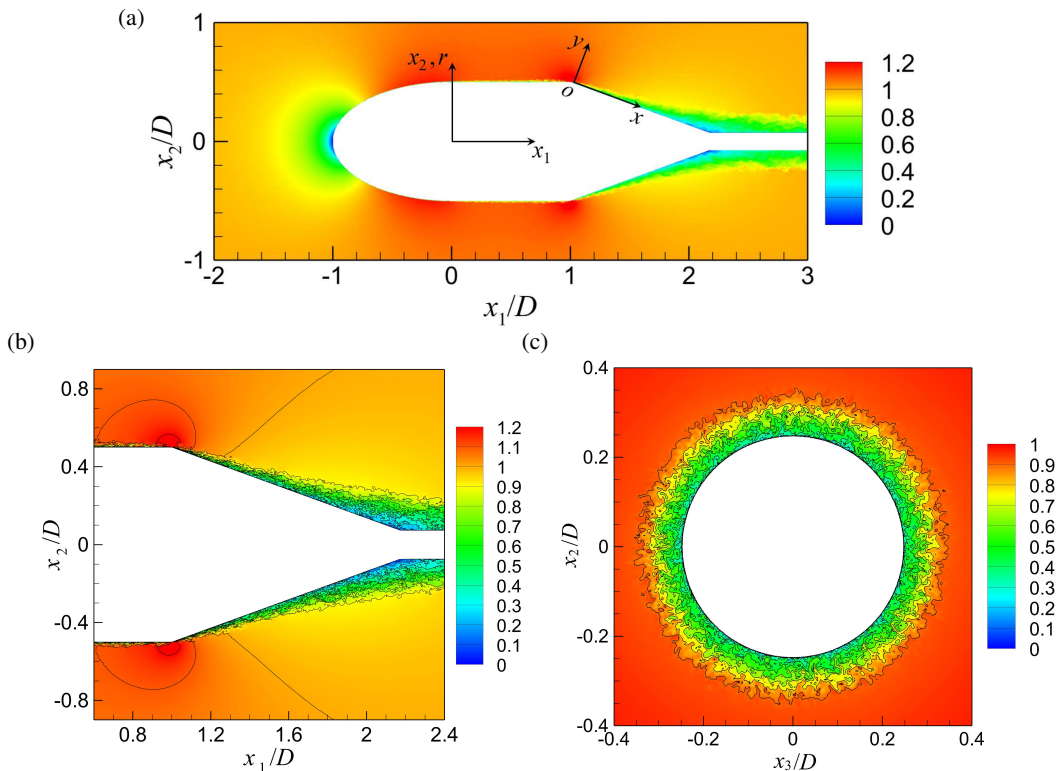


Figure 2: Isocontours of instantaneous axial velocity u_1/U_∞ in (a) the $x_3 = 0$ plane; (b) the $x_3 = 0$ plane around the tail cone; (c) the $x_1/D = 1.69$ plane. Part (a) also illustrates the coordinate systems employed in this study.

the streamwise direction. In total, the coarse mesh contains 3.43×10^8 cells, and the fine mesh has 9.16×10^8 cells.

A maximum Courant–Friedrichs–Lewy number of 1.8 is employed for time advancement in all simulations. This corresponds to time step sizes of $\Delta t U_\infty / D \approx 1.32 \times 10^{-4}$ for the coarse mesh and 8.96×10^{-5} for the fine mesh. The simulations are first run for over one and half flow-through times ($16.8D/U_\infty$) to wash out initial transients, and then another two flow-through times ($22.3D/U_\infty$) to obtain converged statistics.

3. Validation

The velocity field around the BOR is illustrated in figure 2 in terms of the instantaneous axial-velocity contours in two perpendicular planes through the BOR axis. The results are obtained from the fine-mesh simulation. The flow accelerates around the nose, transitions quickly to turbulence after the trip ring at the downstream end of the nose, and accelerates again as it approaches the sharp corner between the centerbody and the tail cone. Downstream of this corner, under the influence of APG, the flow decelerates over the tail cone, causing a rapid thickening of the boundary layer. Notably, the tail-cone TBL remains attached except for a very small separation (too small to be seen in the figure) immediately after the corner, which is consistent with the observations in the VT experiment (Balantrapu *et al.* 2021).

In figure 3, the axial distribution of the mean pressure coefficient, $C_p = (P_w - P_\infty) / (\frac{1}{2} \rho U_\infty^2)$, on the BOR is compared with the experimental data of Balantrapu *et al.* (2021). The reference pressure P_∞ is taken at the inlet near the radial boundary. The

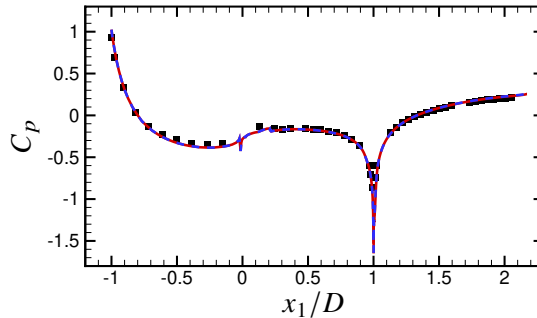


Figure 3: Mean pressure coefficient on the BOR: —, fine mesh; - - -, coarse mesh; ■, experiment (Balantrapu *et al.* 2021)

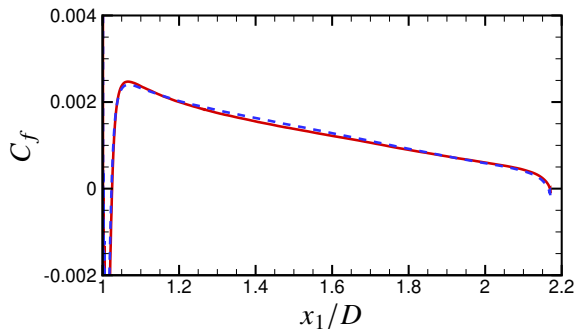


Figure 4: Mean skin-friction coefficient on the tail cone of the BOR: —, fine mesh; - - -, coarse mesh.

distributions obtained from the two simulations are indistinguishable and agree well with the experimental data. The C_p distribution illustrates a strong favorable pressure gradient in the nose region and immediately upstream of the centerbody-tail cone corner. Downstream of the corner, the flow is first subjected to a very strong APG, followed by a more mild APG over the majority of the tail cone. The small kink seen at $x_1/D \approx 0$ is caused by the transition trip. Figure 4 shows the axial distribution of the mean skin-friction coefficient, $C_f = \tau_{w,x}/(\frac{1}{2}\rho U_\infty^2)$, on the tail-cone section of the BOR, where $\tau_{w,x}$ is the mean streamwise shear stress on the wall. A tiny separation bubble with negative C_f is observed at the beginning of the tail cone, and differences between the results from the two meshes are very small, indicating that grid convergence has been achieved.

Figure 5 shows the root-mean-square (r.m.s.) values of pressure fluctuations p'_w on the tail-cone surface. The results from coarse- and fine-mesh simulations again agree well with each other and with the experimental data of Balantrapu *et al.* (2023). The frequency spectra of pressure fluctuations at two axial locations on the tail-cone surface, $x/D = 1.53$ and 1.76 , are shown in figure 6. The simulations predict the wall-pressure fluctuations well over nearly the entire frequency range compared with the experimental data (Balantrapu *et al.* 2023). The grid resolution effect is small and mainly affects the high-frequency content.

A comparison of boundary layer profiles with the measurements of Balantrapu *et al.* (2021) is made in figure 7, where the profiles of mean axial velocity U_1 and r.m.s. values of both axial ($u'_{1,rms}$) and azimuthal ($u'_{\theta,rms}$) velocity fluctuations are depicted at three axial stations on the tail cone. The numerical profiles demonstrate grid convergence and are in reasonable agreement with the measurement data obtained using a four-sensor hot-wire (Balantrapu *et al.* 2021). These results show quantitatively the flow deceleration and boundary-layer thickening

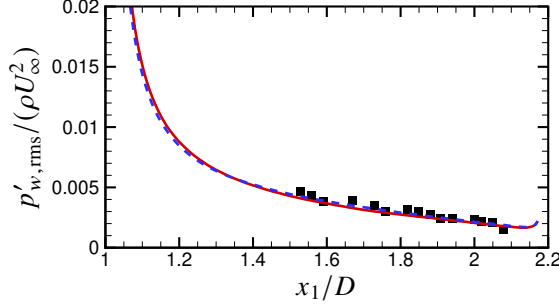


Figure 5: R.M.S. values of pressure fluctuations on the tail-cone surface: —, fine mesh; - - -, coarse mesh; ■, experiment (Balantrapu *et al.* 2023).

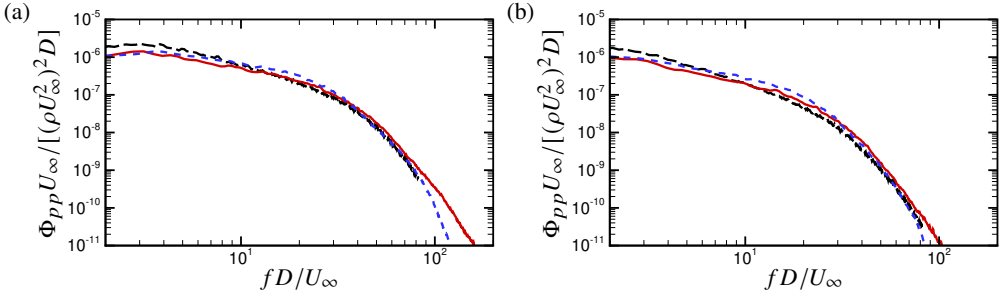


Figure 6: Frequency spectra of surface-pressure fluctuations on the tail cone at: (a) $x_1/D = 1.53$; (b) $x_1/D = 1.76$. —, fine mesh; - - -, coarse mesh; - - -, experiment (Balantrapu *et al.* 2023).

along the tail cone. At the downstream end of the tail cone, $x_1/D = 2.17$, the boundary-layer thickness reaches nearly one half of the BOR radius R , or approximately ten times the boundary-layer thickness immediately upstream of the tail cone. As the TBL develops along the tail cone with decreasing radius, the peak turbulence intensities shift towards the outer region of the boundary layer and the axisymmetric TBL behaves increasingly like an axisymmetric wake.

The frequency spectra of axial and azimuthal velocity fluctuations at two radial locations at the tail-cone end are shown in figure 8. The simulation results exhibit good agreement with the experimental data of Balantrapu *et al.* (2021; private communication 2019) except at high frequencies, where the spectral content is limited by grid resolution and the fine-mesh simulation produces a better comparison. In figure 9, the two-point correlation coefficients of the streamwise velocity fluctuations u' anchored at two radial positions at the end of the tail cone are compared with the single hot-wire data of Balantrapu *et al.* (2021). The two-point correlation coefficients are calculated from

$$C_{uu}(x_1, r, \Delta r, \Delta\theta) = \frac{\overline{\langle u'(x_1, r, \theta, t) u'(x_1, r + \Delta r, \theta + \Delta\theta, t) \rangle}}{\sqrt{\overline{\langle u'^2(x_1, r, \theta, t) \rangle}} \sqrt{\overline{\langle u'^2(x_1, r + \Delta r, \theta + \Delta\theta, t) \rangle}}}, \quad (3.1)$$

where the angle brackets denote spatial averaging over the homogeneous azimuthal direction, and the overbar denotes temporal averaging. The computed results, obtained from the fine-mesh simulation, agree well with the experimental data (Balantrapu *et al.* 2021). They illustrate that variations in correlation length scales along the radial direction is small. More comprehensive discussions of the spatial correlations and turbulence structures are presented in §4.4.

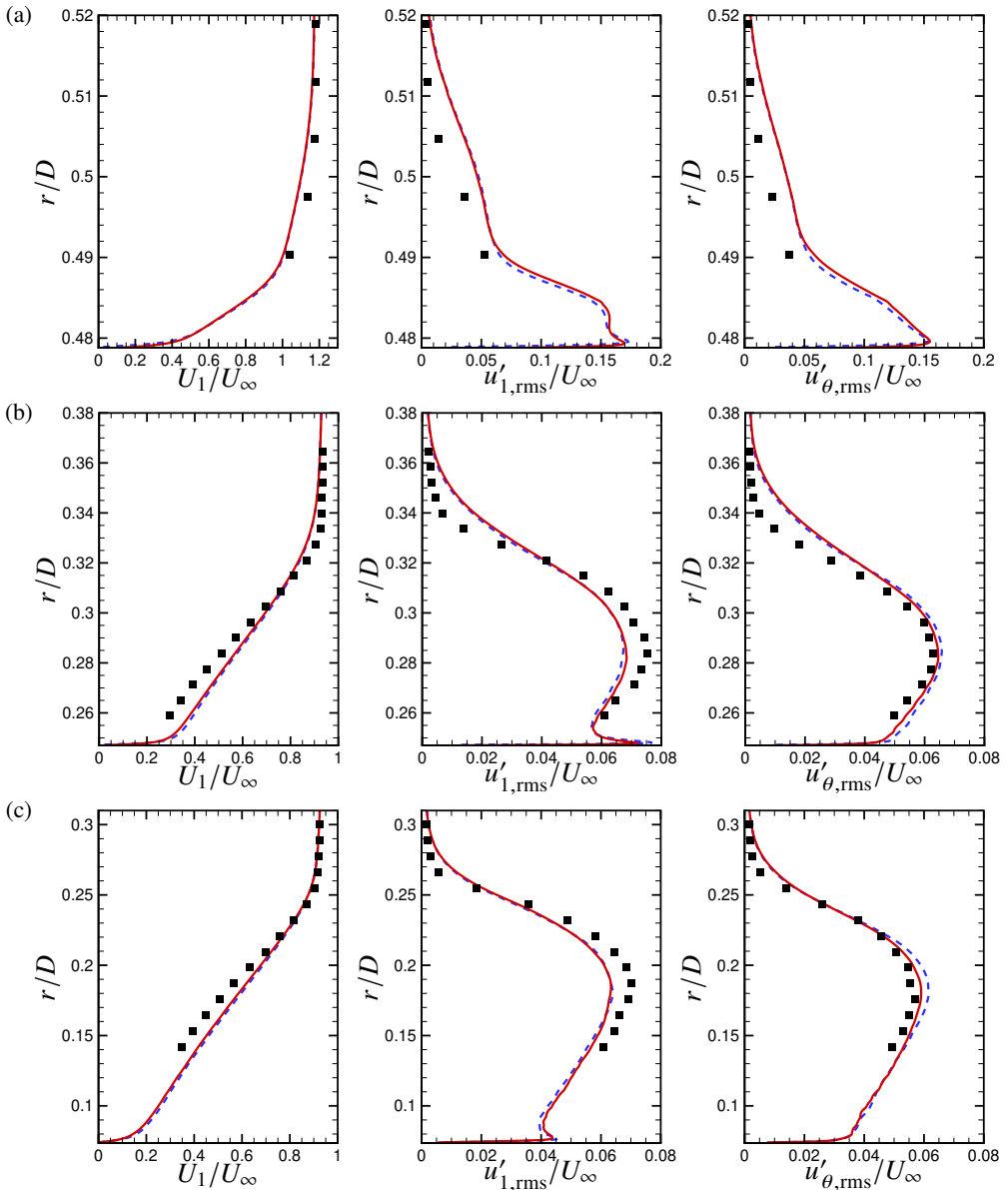


Figure 7: Profiles of mean axial velocity and the r.m.s. values of axial and azimuthal velocity fluctuations at: (a) $x_1/D = 1.06$; (b) $x_1/D = 1.69$; (c) $x_1/D = 2.17$. —, fine mesh; - - -, coarse mesh; ■, experiment (Hickling *et al.* 2019).

In summary, the simulation results presented hitherto demonstrate good agreement with experimental data in terms of the first and second order statistics as well as the space-time characteristics of the tail-cone TBL. Furthermore, they demonstrate grid convergence for all the quantities examined. The comprehensive validation establishes the validity and accuracy of the simulation data, allowing a detailed analysis of the statistics and structure of the axisymmetric tail-cone TBL and their evolution under the APG.

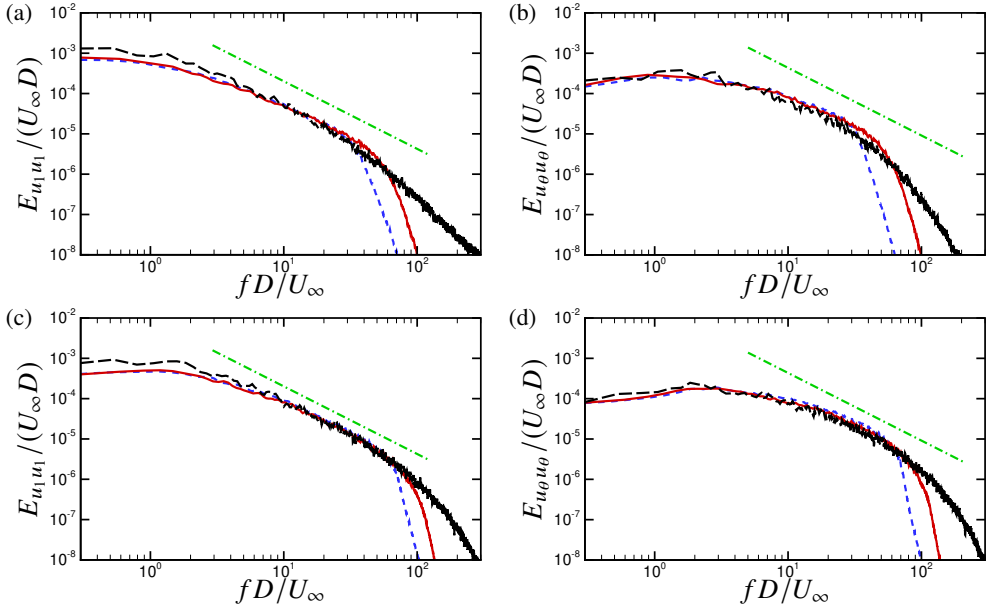


Figure 8: Frequency spectra of fluctuating axial (a,c) and azimuthal (b,d) velocities at two radial locations at the tail-cone end, $x_1/D = 2.17$: (a,b) $r/D = 0.14$; (c,d) $r/D = 0.21$. —, fine mesh; - - -, coarse mesh; —, experiment (Hickling *et al.* 2019); - - -, $-5/3$ slope.

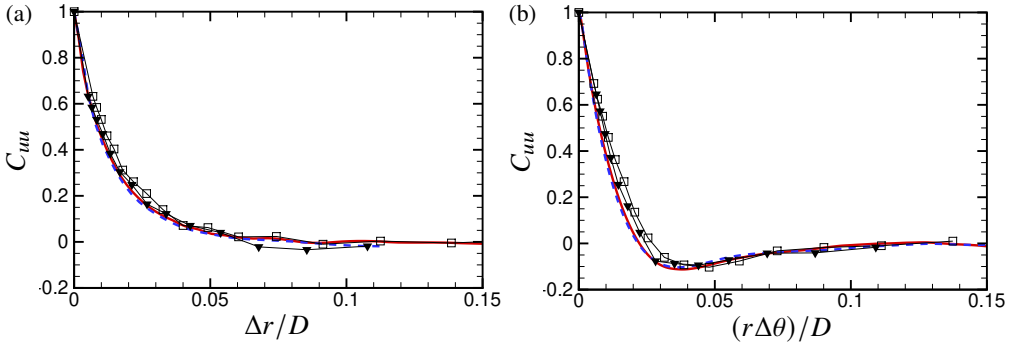


Figure 9: Two-point correlation coefficients of fluctuating streamwise velocity anchored at two radial positions at the tail-cone end ($x_1/D = 2.17$): (a) as a function of radial separation $\Delta r/D$; (b) as a function of azimuthal separation $(r\Delta\theta)/D$. —, LES for $r/D = 0.14$; - - -, LES for $r/D = 0.21$; \square , experiment for $r/D = 0.14$ (Balantrapu *et al.* 2021); \blacktriangledown experiment for $r/D = 0.21$ (Balantrapu *et al.* 2021).

4. Analysis of the tail-cone turbulent boundary layer

Following the convention, results are presented in the boundary-layer coordinate system x - y shown in figure 2a, where x is along the cone surface in the flow direction, y is normal to the surface, and the origin is located at the start of the tail cone. This eliminates any ambiguity that may arise from use of the axial-radial coordinates as in Balantrapu *et al.* (2021). The x -component of velocity is denoted by u and the y -component is v . They are related to the axial velocity u_1 and radial velocity u_r through

$$u = u_1 \cos \alpha - u_r \sin \alpha, \quad v = u_1 \sin \alpha + u_r \cos \alpha \quad (4.1)$$

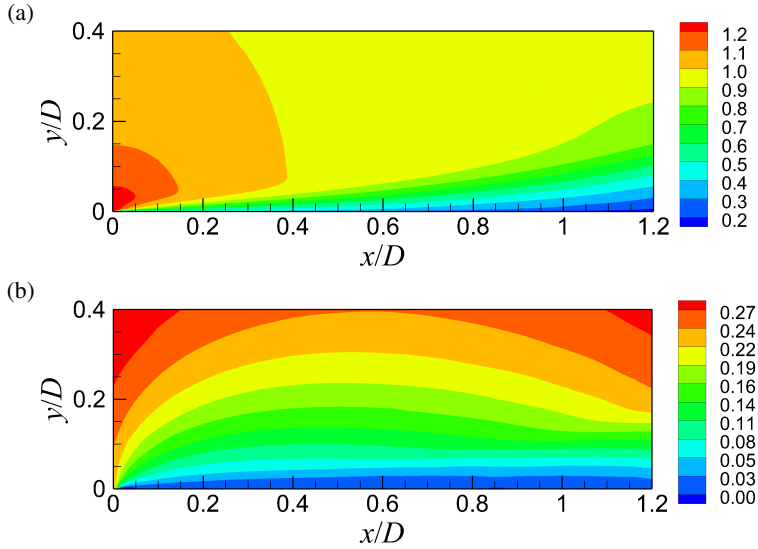


Figure 10: Mean velocity contours in the tail-cone TBL: (a) streamwise velocity U/U_∞ ; (b) wall-normal velocity V/U_∞ .

where $\alpha = 20^\circ$ is the half apex angle of the tail cone. The third velocity component, u_θ , is the same as in the original coordinate systems. All the analyses henceforth are based on data from the fine-mesh simulation.

4.1. Boundary-layer properties and velocity statistics

Figure 10 shows isocontours of the streamwise and wall-normal velocity components in the tail-cone TBL. The flow decelerates along the cone as the boundary-layer thickness grows rapidly. Compared to ZPG flat-plate boundary layers, the wall-normal velocity is larger and varies more significantly within the boundary layer, particularly near the beginning and end of the tail cone due to flow turning following the BOR surface. The subsequent flow analyses is focusing on the region between $0.2 \leq x/D \leq 1$, which excludes the flow deflection regions near both ends of the tail cone.

The streamwise variations of the boundary-layer thickness δ , displacement thickness δ_1 and momentum thickness δ_2 are depicted in figure 11a. It can be noticed that their growth is not linear with the streamwise distance. At $x/D = 1$, the values of δ , δ_1 and δ_2 are approximately 4 times of those at $x/D = 0.2$. The distributions of the friction Reynolds number Re_τ and the momentum thickness Reynolds number Re_{δ_2} are shown in figure 11b, and the boundary-layer shape factor $H = \delta_1/\delta_2$ is displayed in figure 11c. The value of H is larger than that in a ZPG flat-plate TBL, and it grows rapidly along the streamwise direction as a result of increasing APG (Harun *et al.* 2011).

Figure 12a shows profiles of the mean static pressure relative to the wall pressure, $(P - P_w)/(\rho U_\infty^2)$, at four streamwise locations. The pressure variations across the TBL are significant, and the pressure at the boundary-layer edge decreases relative to the local wall pressure in the downstream direction, indicating that the edge pressure rises more slowly than the wall pressure under the APG. The pressure gradient in a boundary layer is commonly characterized by the Clauser pressure-gradient parameter, $\beta = (dP_e/dx)\delta_1/\tau_{w,x}$, where P_e is the mean pressure at the edge of the boundary layer and $\tau_{w,x}$ is the mean wall-shear stress along the surface. For a thin boundary layer, the Clauser parameter can be equivalently evaluated based on the mean wall pressure P_w since the pressure change

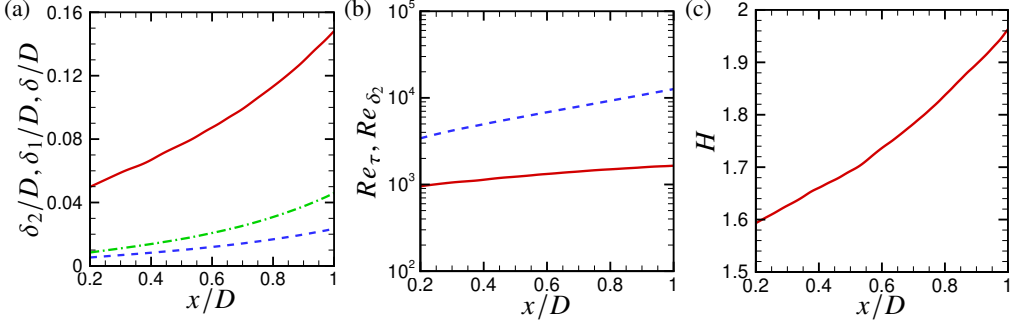


Figure 11: Distributions of boundary-layer parameters: (a) boundary-layer thickness δ (—), displacement thickness δ_1 (- - -) and momentum thickness δ_2 (- - -); (b) Reynolds numbers Re_τ (—) and Re_{δ_2} (- - -); (c) shape factor H .

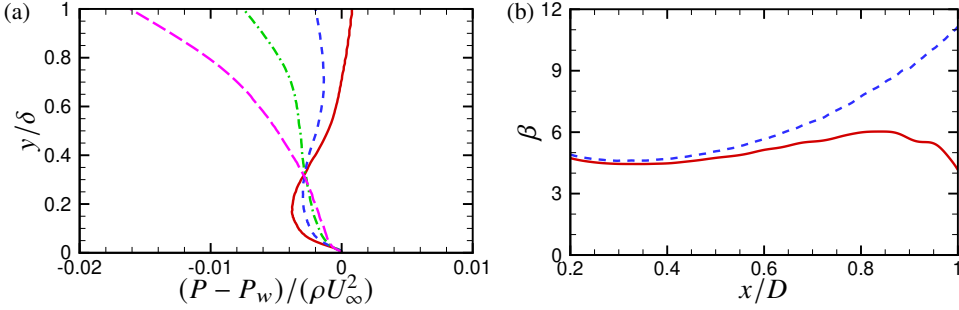


Figure 12: (a) Profiles of mean pressure relative to the local wall pressure across the boundary layer at four streamwise locations: —, $x/D = 0.21$; - - -, $x/D = 0.43$; - · - ·, $x/D = 0.71$; - - - -, $x/D = 0.99$. (b) Streamwise variations of the Clauser pressure gradient parameter β : —, based on the mean pressure at the edge of the boundary layer; - - -, based on the mean wall pressure.

across the boundary layer is small. However, this is not the case for the rapidly thickening boundary layer considered here. The streamwise evolutions of β calculated based on P_e and P_w are shown in figure 12b. The values of β are high overall, which verifies that the flow is under strong APG. The two definitions give similar β values in the upstream portion of the boundary layer where it is relatively thin, but their difference increases towards downstream as the boundary layer thickens. The β based on P_e increases from 4.7 at $x/D = 0.2$ to a peak value of 6.1 at $x/D = 0.85$, and then declines to 4.2 at $x/D = 1.0$. In contrast, the β based on P_w increases nearly monotonically from 4.9 to 11.1. The smaller pressure gradient outside the thick TBL is consistent with the earlier findings of Patel *et al.* (1974).

The decreasing radius of the tail cone in the downstream direction can also potentially influence the evolution of the TBL, and thus the transverse curvature effect on the TBL is evaluated. As pointed out by Piquet & Patel (1999), the strength of the transverse curvature effect can be estimated based on two parameters, the radius of the surface curvature in inner scale, $r_s^+ = u_\tau r_s / \nu$, and the ratio of the boundary-layer thickness to the surface radius, δ/r_s . The distributions of r_s^+ and δ/r_s along the tail-cone are shown in figure 13. It can be noticed that δ/r_s increases quickly in the second half of the region, but its value remains less than 1 within the region of analysis. Conversely, the value of r_s^+ declines continuously and its smallest value is approximately 1700. According to the review by Piquet & Patel (1999), in flows characterized by large r_s^+ and small (or order one) δ/r_s values, the impact of transverse

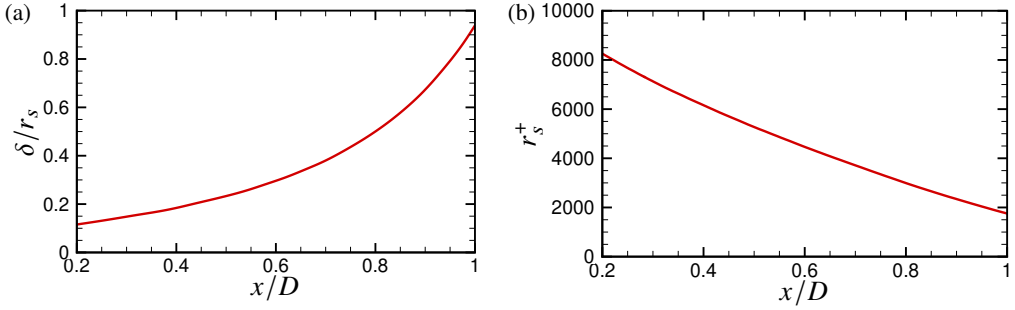


Figure 13: Distributions of transverse curvature parameters along the tail cone: (a) δ/r_s ; (b) r_s^+ .

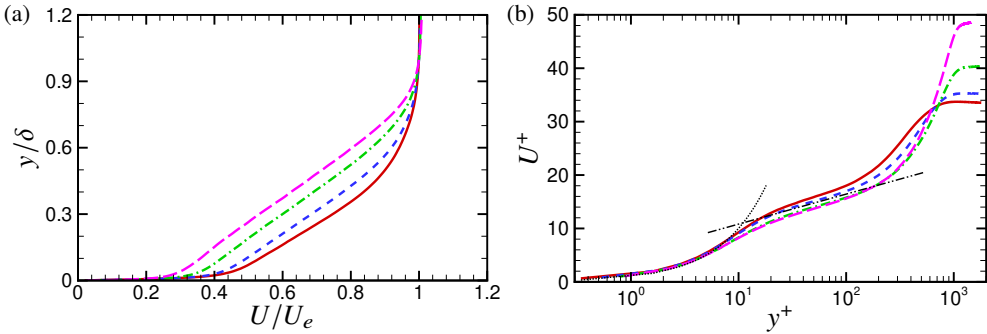


Figure 14: Mean streamwise velocity profiles with (a) outer scaling and (b) inner scaling at four streamwise locations: —, $x/D = 0.21$; - - -, $x/D = 0.43$; ····, $x/D = 0.71$; - · - ·, $x/D = 0.99$. In (b): ·····, $U^+ = y^+$; - · - ·, $U^+ = (1/\kappa) \ln(y^+) + B$ with $\kappa = 0.41$ and $B = 5.2$.

curvature on the boundary layer is small and primarily felt in the outer layer. It can therefore be reasonably assumed that the effect of transverse curvature is small in the present TBL relative to the influence of the APG.

The outer- and inner-scaled mean streamwise velocity profiles at four streamwise stations are shown in figures 14a and 14b, respectively. In figure 14a, the velocity is scaled by the local mean streamwise velocity U_e at the edge of the boundary layer, and the y -coordinate is scaled by the local boundary-layer thickness δ . The profiles become less full in the downstream direction, which is consistent with the monotonic increase of shape factor in figure 11c. Despite the presence of strong APG, the boundary layer remains attached at all four locations and through the end of the tail cone. In Figure 14b, the velocity is scaled by the local friction velocity u_τ , and the y -coordinate is scaled using the viscous length scale ν/u_τ . The inner-scaled profiles collapse within the viscous sublayer onto the linear law. Moreover, each profile features a noticeable logarithmic region extending from $y^+ \approx 30$ to 130, which is narrower than that of a canonical ZPG planar TBL. In comparison with the classical log law, $U^+ = (1/\kappa) \ln(y^+) + B$ with $\kappa = 0.41$ and $B = 5.2$, these profiles exhibit a slightly steeper slope. At the two downstream stations, the velocity profiles fall below the standard log law due to the increasing β value. These changes in the log region are consistent with the results of some previous studies of APG TBLs (Nagano *et al.* 1998; Monty *et al.* 2011). In the wake region U^+ rises faster and attains higher values at downstream locations.

Figure 15 presents the r.m.s. values of velocity fluctuations u' , v' , u'_θ and the Reynolds shear stress $\overline{u'v'}$ with outer scaling at the same four x -locations. A near-wall peak, henceforth

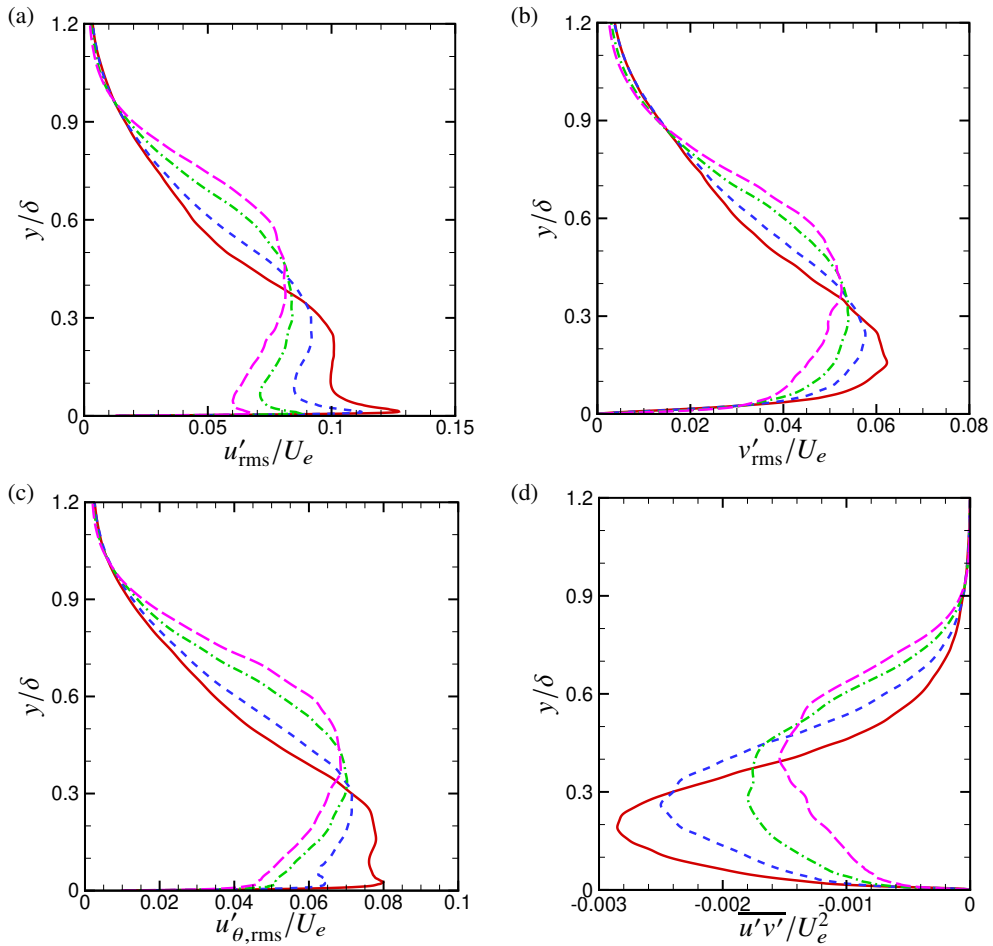


Figure 15: Profiles of (a-c) r.m.s. values of velocity fluctuations and (d) Reynolds shear stress with outer scaling at: —, $x/D = 0.21$; - - -, $x/D = 0.43$; - · - ·, $x/D = 0.71$; · · · ·, $x/D = 0.99$.

referred to as the inner peak, is observed in the profiles of both the streamwise and azimuthal velocity components. This peak becomes weaker in the downstream direction and, in the case of the azimuthal velocity, vanishes at the last two stations plotted. Note that the inner peak was not captured in the measurement of Balantrapu *et al.* (2021) due to its close proximity to the wall. On the other hand, a broader peak can be found in all r.m.s. profiles in the wake region of the TBL. Similar to the inner peak, the strength of the outer peak also decreases, albeit more slowly, in the downstream direction. However, this is accompanied by an outward shift and broadening of the peak, resulting in a growth of turbulence intensity in the outer region of $0.4 \lesssim y/\delta \lesssim 0.9$. In figure 16, the same velocity r.m.s. and Reynolds shear-stress profiles are plotted with inner scaling. They exhibit a degree of self-similarity within the very near-wall region ($y^+ < 10$), a characteristic also observed in the inner-scaled mean streamwise velocity profiles. The inner peaks in the streamwise and azimuthal velocity fluctuations are located at $y^+ \approx 12$ and $y^+ \approx 25$, respectively. While their strengths decrease in the streamwise direction, the locations of the inner peaks remain unchanged in wall units. Conversely, the outer peaks move further outward with increasing strength and width as x/D increases. The appearance of outer peaks in turbulence intensity profiles is a general

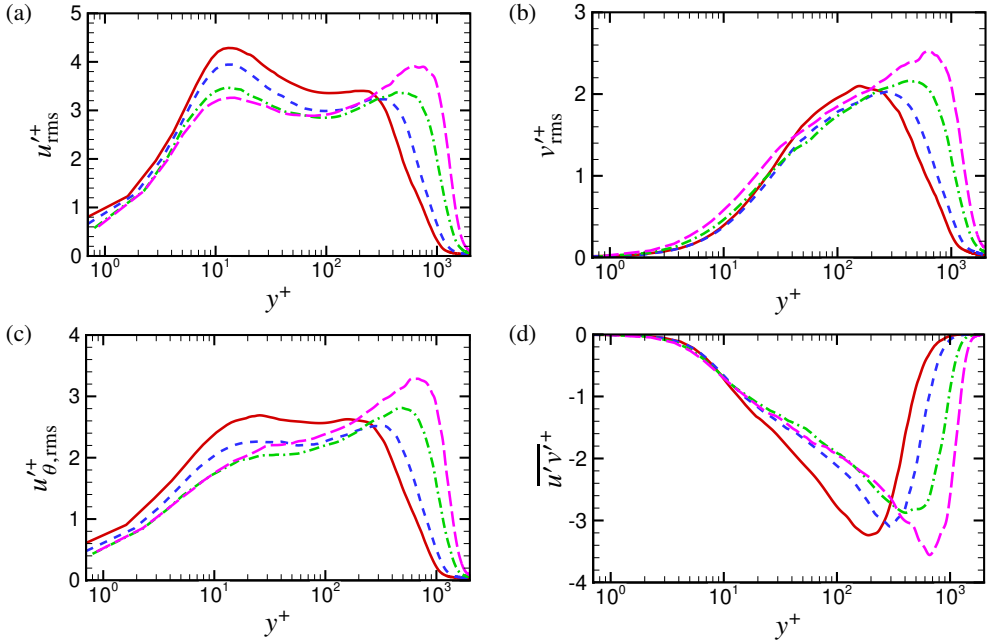


Figure 16: Profiles of (a-c) r.m.s. values of velocity fluctuations and (d) Reynolds shear stress with inner scaling at: —, $x/D = 0.21$; - - -, $x/D = 0.43$; - · - ·, $x/D = 0.71$; · · · ·, $x/D = 0.99$.

feature of TBLs with APG, which energizes large-scale motions (Monty *et al.* 2011). More discussions about energy distributions in the boundary layer are provided in Section 4.3.

4.2. Self-similarity with embedded-shear-layer scaling

The results in the previous section show a lack of self-similarity in velocity statistics profiles with either inner scaling or outer scaling with δ as the length scale, which is expected given the highly nonequilibrium nature of the boundary layer. Balantrapu *et al.* (2021) showed improved outer-scaling using the displacement thickness as the length scale, but the degree of profile collapse is still limited. They subsequently demonstrated good self-similarity by using the embedded-shear-layer scaling proposed by Schatzman & Thomas (2017). In this section, the validity of embedded-shear-layer scaling for the present axisymmetric APG TBL is further evaluated using the LES data, which include all three velocity components.

Based on the embedded-shear-layer scaling (Schatzman & Thomas 2017), the similarity variables are $\eta = (y - y_{IP})/\delta_\omega$ and $U^* = (U_e - U)/U_d$, where the subscript IP denotes the outer inflection point of the mean streamwise velocity profile, $\delta_\omega = (U_e - U)_{IP}/(dU/dy)_{IP}$ is the local vorticity thickness of the embedded shear layer, and $U_d = (U_e - U)_{IP}$ is the local mean streamwise velocity defect at the inflection point. In figure 17, the mean streamwise velocity profiles in figure 14 are presented in terms of the embedded-shear-layer scaling. The location $\eta = 0$ corresponds to the outer inflection point in the mean streamwise velocity profile. All four profiles show good similarity over a wide range of the wall-normal distance except in the vicinity of the wall due to the wall effect. This confirms the scaling results of Balantrapu *et al.* (2021), whose experimental data does not include the near-wall region, and is consistent with the data of Schatzman & Thomas (2017) for the APG TBLs on a 2-D hump. As the location moves downstream, the self-similar behavior extends further toward the wall in the η -coordinate. In addition, the self-similar profiles are seen to collapse well

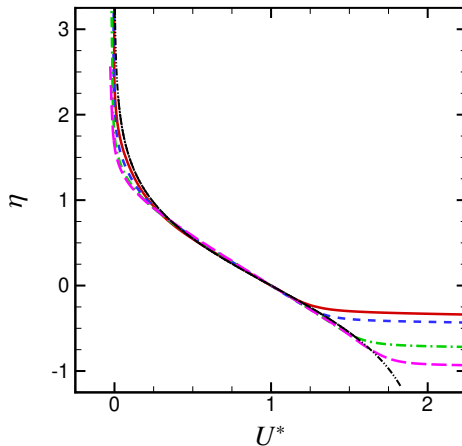


Figure 17: Mean streamwise velocity profiles with embedded-shear-layer scaling (Schatzman & Thomas 2017) at four streamwise positions: —, $x/D = 0.21$; - - -, $x/D = 0.43$; - · - ·, $x/D = 0.71$; · · · ·, $x/D = 0.99$. The line - - - represents the function $U^* = 1 - \tanh(\eta)$.

onto the function $U^* = 1 - \tanh(\eta)$, and the η -range of collapse also expands along the streamwise direction.

Figure 18 displays the r.m.s. values of the three components of velocity fluctuations and the Reynolds shear stress $\overline{u'v'}$ with the embedded-shear-layer scaling. The profiles of all three r.m.s. velocity components exhibit some degree of similarity in the region above the inflection point ($\eta \geq 0$), similar to that shown by Balantrapu *et al.* (2021) with single-hotwire velocity data. The failure of the shear-layer scaling in the near-wall region is again expected due to the wall effect, and the larger deviations of the profiles at $x/D = 0.21$ near the inflection point result from the influence of the upstream corner flow at the beginning of the cone, where the pressure gradient is extremely large and varies rapidly (cf. figure 3). Similarity in velocity fluctuations is improved at the downstream stations as the APG variation becomes more mild. Furthermore, it is worth noting that the outer peaks in the r.m.s. velocity profiles are all located at $\eta \approx 0.2$, which is slightly above the inflection point, and the peak values relative to the mean streamwise velocity defect remain relatively constant. The peaks in the streamwise-component profiles are $u'_{rms}/U_d \approx 0.21$, which is consistent with Balantrapu *et al.* (2021) and the values for the APG TBLs on a 2-D ramp investigated by Schatzman & Thomas (2017). Large deviations are observed among the different Reynolds shear-stress profiles around their peaks, suggesting a more restricted region of validity of embedded-shear-layer scaling.

4.3. Azimuthal wavenumber spectra of streamwise velocity fluctuations

The profiles of velocity fluctuations in figure 16 provide an overall measure of the energy distributions within the TBL. To explore the evolution of energy distribution among different length scales, the pre-multiplied azimuthal wavenumber spectra of the streamwise velocity fluctuations, $k_\theta \phi_{uu}(k_\theta)/u_\tau^2$, are examined. Figure 19 shows the pre-multiplied spectra as a function of y^+ and the azimuthal wavelength in wall units, $\lambda_\theta^+ = (2\pi/k_\theta)(u_\tau/\nu)$, at the four streamwise locations. It can be observed that there are two energy peaks at different wall-normal locations, which is consistent with the r.m.s. results shown in figure 16a. The azimuthal wavelengths and the wall-normal locations of these two peaks are marked in the figure. The first peak, located at $y^+ \approx 12$ with azimuthal wavelengths of 110 to 135 wall units, is called the inner peak and is associated with elongated near-wall streaks. While

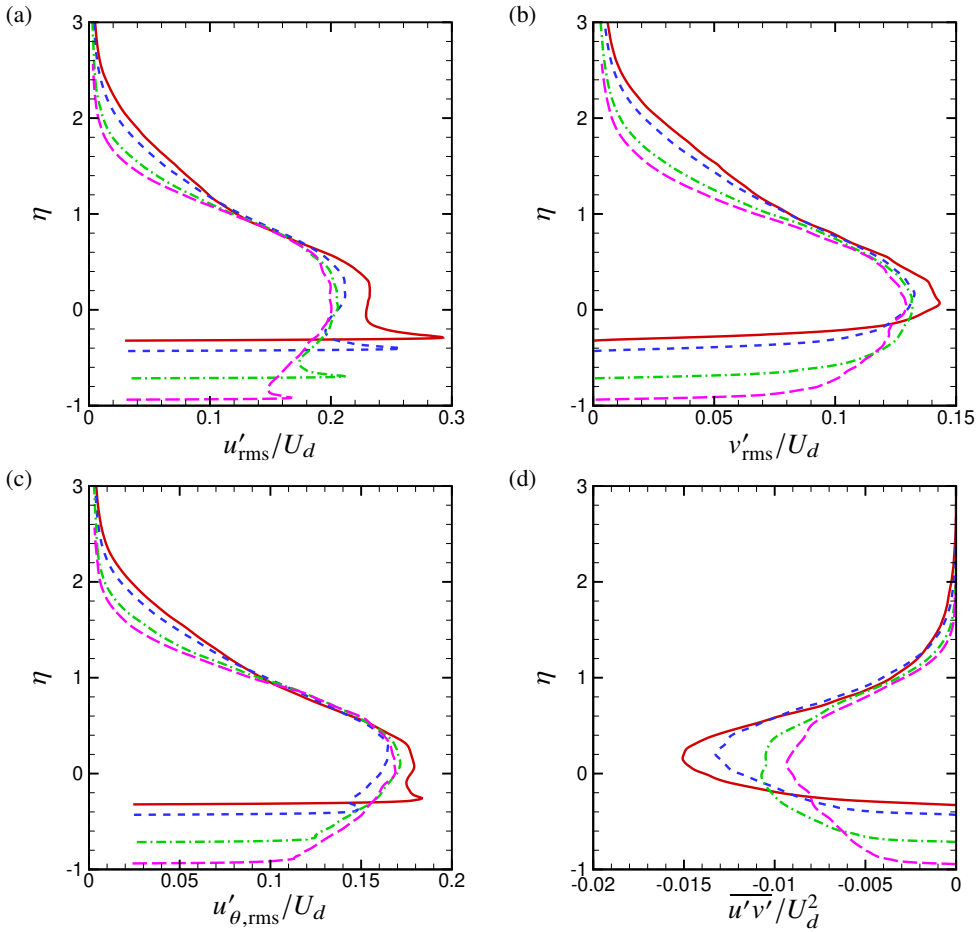


Figure 18: Profiles of (a-c) r.m.s. values of the three components of velocity fluctuations and (d) the Reynolds shear stress $\overline{u'v'}$ with embedded-shear-layer scaling at: —, $x/D = 0.21$; - - -, $x/D = 0.43$; ···, $x/D = 0.71$; - · - ·, $x/D = 0.99$.

the azimuthal wavelength of the inner peak, and hence the spacing between the streaks in wall units are slightly decreased in the downstream direction, they are not significantly different from those in ZPG flat-plate TBLs. This is consistent with the experimental results of Harun *et al.* (2013) but contrary to the findings of Lee & Sung (2009) from DNS of an APG flat-plate TBL at a lower Reynolds number. The latter showed a significant increase in the spanwise spacing between streaks under the influence of a strong APG. It can also be noted from figure 19 that although the positions of the inner peaks are similar at different streamwise locations, the strengths of the peaks decrease rapidly in the downstream direction.

The secondary peak in the azimuthal wavenumber spectra, referred to as the outer peak, is located in the wake region of the TBL, which is different from that for a ZPG TBL (Mathis *et al.* 2009; Wang *et al.* 2018). As the TBL evolves toward downstream, the azimuthal wavelength of the outer peak and its distance to the wall both grow, indicating that increasingly larger-scale structures further away from the wall are energized. However, the growth of the azimuthal length scale becomes slower in the downstream. The azimuthal wavelength normalized by the outer length scale, λ_θ/δ , is around 0.4, which is smaller than the spanwise length scale in ZPG flat-plate TBLs (e.g., ≈ 0.9 in Wang *et al.* (2018)). Furthermore, the

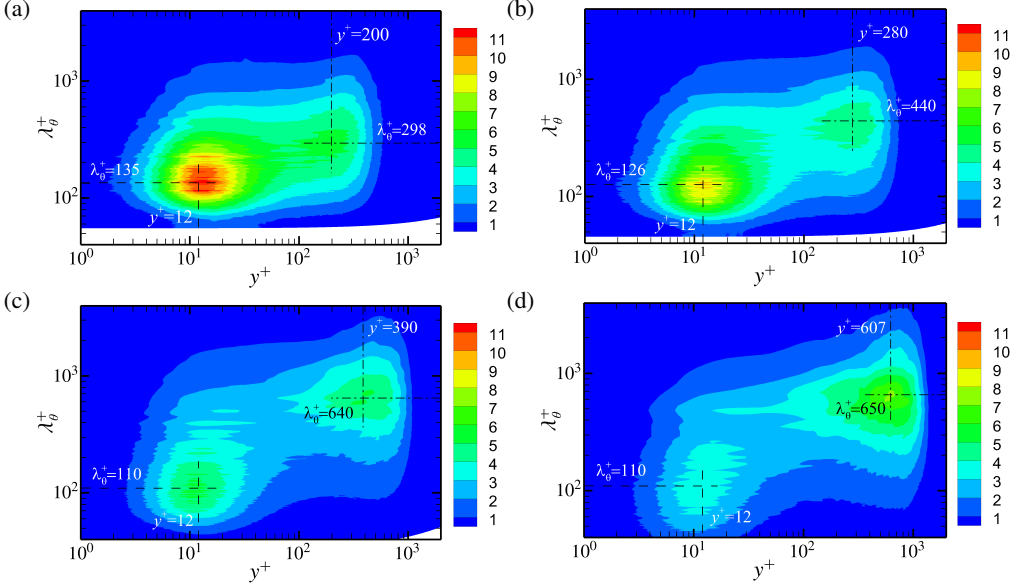


Figure 19: Pre-multiplied energy spectra $k_\theta \phi_{uuu}/u_\tau^2$ as a function of the wall-normal coordinate and azimuthal wavelength in wall units at: (a) $x/D = 0.21$, (b) $x/D = 0.43$, (c) $x/D = 0.71$ and (d) $x/D = 0.99$. The intersections of the dashed lines and dash-dotted lines indicate the approximate locations of the inner and outer peaks, respectively.

strength of the outer peak increases gradually toward downstream, in agreement with the trend for the turbulence intensity and Reynolds shear stress seen in figure 16.

4.4. Two-point correlations of streamwise velocity fluctuations

In this section, the structure of the tail-cone TBL is discussed further in terms of two-point spatial correlations. Figure 20 shows the two-point correlations of the streamwise velocity fluctuations in the streamwise-wall-normal (x - y) and cross-flow (y - θ) planes anchored at the previous four streamwise stations with $y/\delta = 0.4$, which is in the vicinity of the outer peaks of the energy spectra. The two-point spatial correlation coefficient C_{uu} is defined as:

$$C_{uu}(x, y, \Delta x, \Delta y, \Delta \theta) = \frac{\overline{\langle u'(x, y, \theta, t) u'(x + \Delta x, y + \Delta y, \theta + \Delta \theta, t) \rangle}}{\sqrt{\overline{\langle u'^2(x, y, \theta, t) \rangle}} \sqrt{\overline{\langle u'^2(x + \Delta x, y + \Delta y, \theta + \Delta \theta, t) \rangle}}}. \quad (4.2)$$

It is independent of the azimuthal angle θ because of spatial homogeneity. The correlation contours illustrate significant growth of turbulence length scales with growing boundary-layer thickness, indicated by the dashed line, in the downstream direction. Moreover, the evolving contour shapes in the x - y plane indicate increasing anisotropy of large-scale structures toward the downstream.

To examine the size, shape and orientation of turbulence structures relative to the boundary-layer thickness, the two-point correlations in the x - y plane in figure 20 are replotted in figure 21 with the coordinates normalized by the local δ . Around all four anchor locations, the high-level contours have similar shapes and orientations while their enclosed areas decrease relative to δ in the downstream direction, indicating that small-scale turbulence is not strongly affected by the boundary-layer deceleration (see also figure 20). On the other hand, the shapes of the lower level contours at larger separations vary greatly with x , becoming more elongated along the major axis of the oval-like contours. The contours span

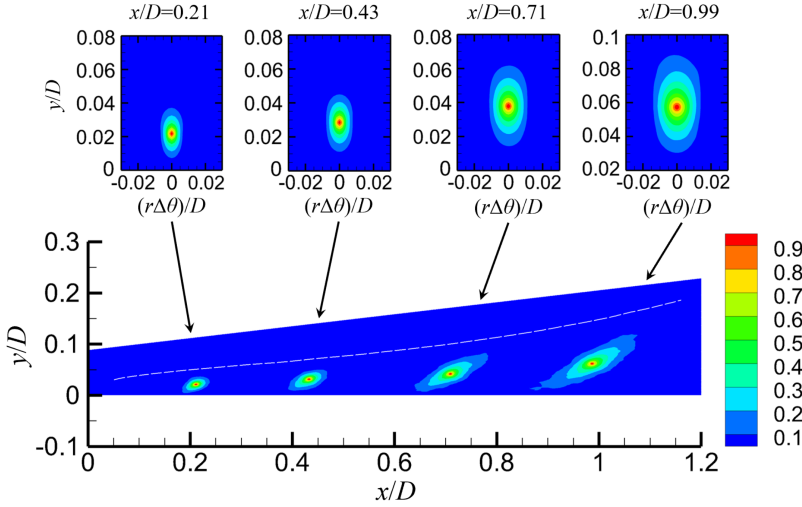


Figure 20: Coefficients of two-point correlations of streamwise velocity fluctuations in the streamwise-wall-normal (x - y) and cross-flow (y - θ) planes with origins at four streamwise stations and $y/\delta = 0.4$. The white dashed line represents the edge of the boundary layer.

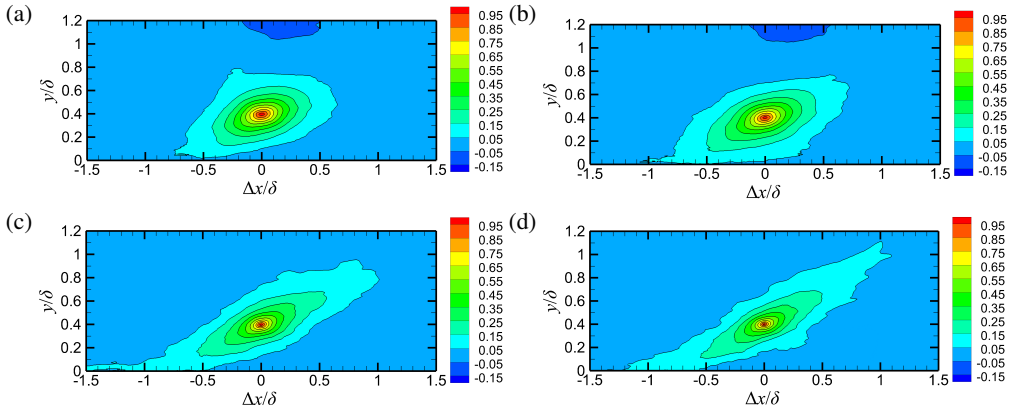


Figure 21: Coefficients of two-point correlations of streamwise velocity fluctuations in the x - y plane with anchor points located at $y/\delta = 0.4$ and (a) $x/D = 0.21$; (b) $x/D = 0.43$; (c) $x/D = 0.71$; (d) $x/D = 0.99$.

a large portion of the boundary layer at each streamwise station, and the correlation lengths relative to δ , estimated by the decay of C_{uu} (e.g., to e^{-1}), are only modestly decreased toward the downstream despite large changes in the low-level contour shapes. Figure 22 shows the two-point velocity correlations closer to the wall at $y/\delta = 0.1$. Compared to their outer-region counterparts in figure 21, the correlation contours are more elongated and lean more toward the wall with smaller inclination angles, which is consistent with the known hairpin vortex structure in TBLs. It should be mentioned that the x - y correlations of the wall-normal and azimuthal velocity components, not shown here for brevity, exhibit the same trend of variations with the streamwise position as the streamwise velocity correlations.

The overall inclination angles of the correlations at $y/\delta = 0.1, 0.2$ and 0.4 are quantified in figure 23 for the four streamwise stations. The angles are determined using the approach proposed by Christensen & Wu (2005) based on a least-squares fit of a line through the

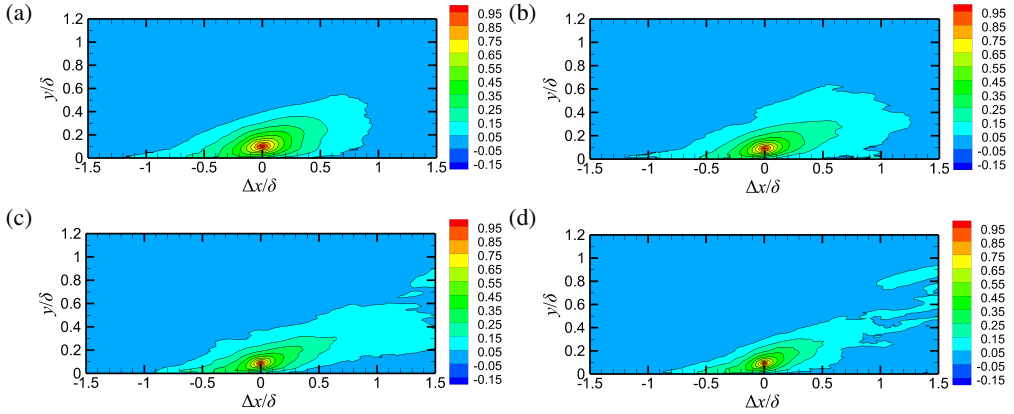


Figure 22: Coefficients of two-point correlations of streamwise velocity fluctuations in the x - y plane with anchor points located at $y/\delta = 0.1$ and (a) $x/D = 0.21$; (b) $x/D = 0.43$; (c) $x/D = 0.71$; (d) $x/D = 0.99$.

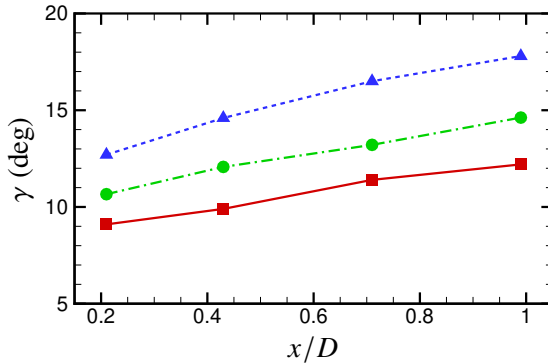


Figure 23: Overall inclination angle γ of C_{uu} contours anchored at four streamwise stations and three wall-normal locations: \blacksquare , $y/\delta = 0.1$; \bullet , $y/\delta = 0.2$; \blacktriangle , $y/\delta = 0.4$.

points farthest upstream and downstream of each of the $C_{uu} = 0.35, 0.45, 0.55, 0.65$ and 0.75 isocontours. The angle between this fitted line and the positive x -axis, γ , is representative of the inclination of the hairpin vortex organization in the TBL (Christensen & Wu 2005). Consistent with the measurements of Volino (2020) for APG TBLs on a 2-D ramp, the results indicate that the inclination angle increases in the downstream direction. At each streamwise station, the inclination angle increases with the wall-normal distance, and its value at $y/\delta = 0.4$ exceeds the typical value of approximately 11° in plane-wall turbulent channel flows and ZPG TBLs at the same position (Christensen & Wu 2005; Sillero *et al.* 2014; Volino 2020). This increase is attributed to the effect of APG (Lee 2017; Volino 2020).

Figure 24 shows δ -scaled streamwise-velocity correlations in the cross-flow plane. As in the x - y plane, the correlation contours exhibit modest decreases in length scales relative to the local boundary-layer thickness in the downstream direction. However, the shapes of the correlation contours, elongated in the wall-normal direction, are very similar at the four locations, in contrast to their counterparts in the x - y plane. Negative lobes are observed on both sides of the positive contours. The distance between alternating positive and negative correlation regions decreases to approximately 0.4δ at the last downstream station, which is much smaller than that in a ZPG flat-plate TBL (Sillero *et al.* 2014).

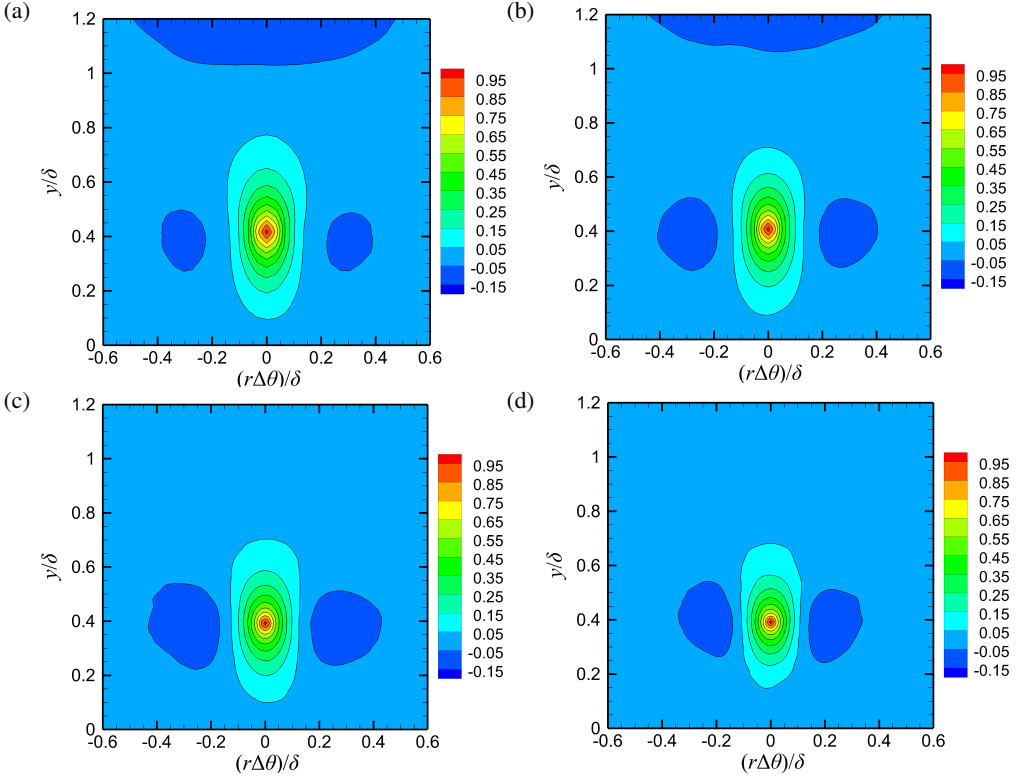


Figure 24: Coefficients of two-point correlations of streamwise velocity fluctuations in y - θ planes with anchor points located at $y/\delta = 0.4$ and (a) $x/D = 0.21$; (b) $x/D = 0.43$; (c) $x/D = 0.71$; (d) $x/D = 0.99$.

The spatial correlations at different positions in the boundary layer are compared more quantitatively in figures 25 and 26. Figure 25 illustrates the correlations anchored at the previous four streamwise locations at $y/\delta = 0.4$ as one-dimensional functions of spatial separations. Each plot corresponds to separation in one direction, and the four curves in each plot represent the four anchor locations. It can be seen that for all anchor locations, the correlation length in the streamwise direction is larger than that in the wall-normal direction (note the different abscissa ranges used in the plots for clarity), and the azimuthal correlation length is the smallest. As the anchor point moves downstream, a reduction in correlation lengths relative to δ is evident in all three directions. In relative terms, the azimuthal correlation is less changed than the correlations in the other two directions. Additionally, as shown in figure 25c the negative lobes in the azimuthal correlations become more pronounced and the separation distance is reduced toward downstream. In figure 26, the one-dimensional correlations anchored at three different wall-normal locations at $x/D = 0.71$ are compared. The correlations are remarkably similar at the three vastly different positions: $y/\delta = 0.1, 0.4$ and 0.7 . For the streamwise correlation, a small reduction with increasing distance to the wall can be noticed at large separations, leading to a small decrease of the correlation length. The correlations in the other two directions barely vary with the wall-normal distance. These findings are consistent with the results of the flat-plate TBL with strong APG reported by Lee (2017).

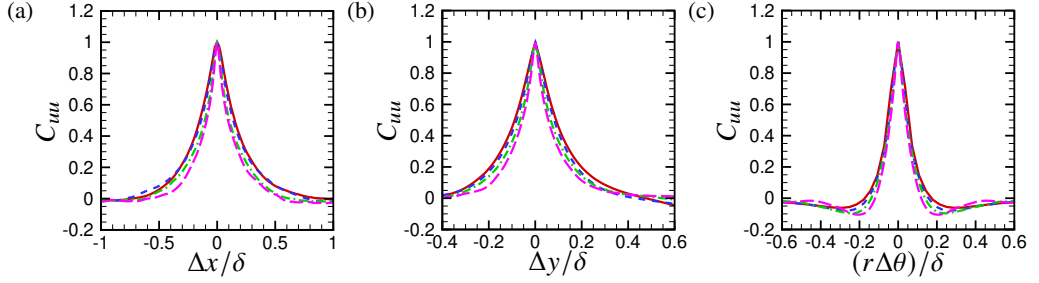


Figure 25: Correlation coefficients of streamwise velocity fluctuations as a function of (a) streamwise separation, (b) wall-normal separation, and (c) azimuthal separation. The lines in each plot represent different anchor locations at $y/\delta = 0.4$ and: —, $x/D = 0.21$; - - -, $x/D = 0.43$; - · - ·, $x/D = 0.71$; - - - -, $x/D = 0.99$.

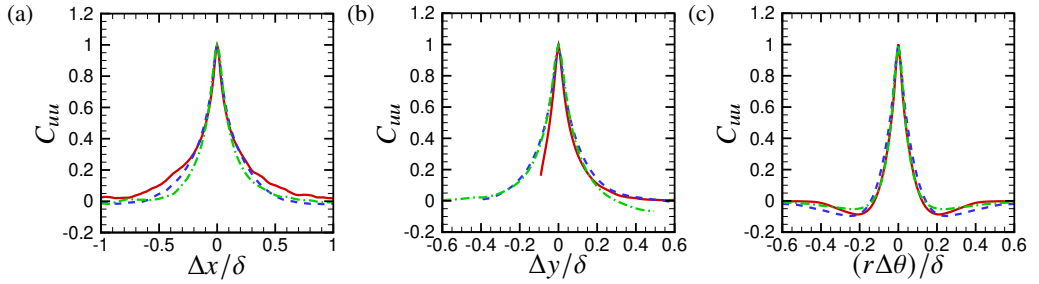


Figure 26: Correlation coefficients of streamwise velocity fluctuations as a function of (a) streamwise separation, (b) wall-normal separation, and (c) azimuthal separation. The lines in each plot represent different anchor locations at $x/D = 0.71$ and: —, $y/\delta = 0.1$; - - -, $y/\delta = 0.4$; - · - ·, $y/\delta = 0.7$.

4.5. Integral length scales

To further elucidate the three-dimensional structure of the boundary layer, the integral lengths (or correlation lengths) along the streamwise, wall-normal and azimuthal directions are evaluated based on the spatial correlations as

$$\Lambda_x = \int C_{uu}(x, y, \Delta x) d(\Delta x), \quad (4.3)$$

$$\Lambda_y = \int C_{uu}(x, y, \Delta y) d(\Delta y), \quad (4.4)$$

$$\Lambda_\theta = \int C_{uu}(x, y, \Delta\theta) r d(\Delta\theta), \quad (4.5)$$

respectively. The integrations are taken between the intersections with $C_{uu} = 0.05$, and in the wall-normal direction it is bounded by $y/\delta = 0$ and 1 at the two ends. This definition is consistent with that used by Sillero *et al.* (2014) to facilitate a comparison with their flat-plate TBL results. Figure 27 shows the outer-scaled integral lengths of the streamwise velocity as functions of the wall-normal distance at four streamwise locations, along with the DNS data of Sillero *et al.* (2014) for a ZPG flat-plate TBL at $Re_\tau = 2000$. The integral lengths in the APG axisymmetric TBL are all markedly shorter than those in the ZPG TBL. Consistent with the observation from figure 25, all the integral lengths decrease in the downstream direction. The wall-normal variations of streamwise and wall-normal integral lengths are similar among the different streamwise locations, and exhibit largely the same trend as those in the ZPG TBL. In the near-wall region, however, the streamwise integral lengths in the

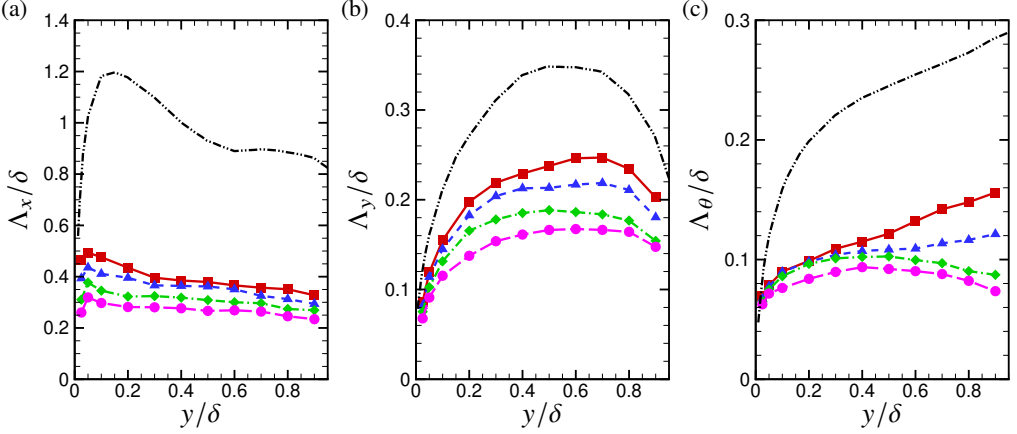


Figure 27: Outer-scaled integral lengths in (a) streamwise, (b) wall-normal, and (c) azimuthal directions as a function of y at four streamwise locations: — with \blacksquare , $x/D = 0.21$; - - - with \blacktriangle , $x/D = 0.43$; - · - · with \blacklozenge , $x/D = 0.71$; - · - · with \bullet , $x/D = 0.99$. The chain-dot-dot lines are from the DNS of a ZPG flat-plate TBL at $Re_\tau \approx 2000$ (Sillero *et al.* 2014), with the azimuthal correlation replaced by spanwise correlation.

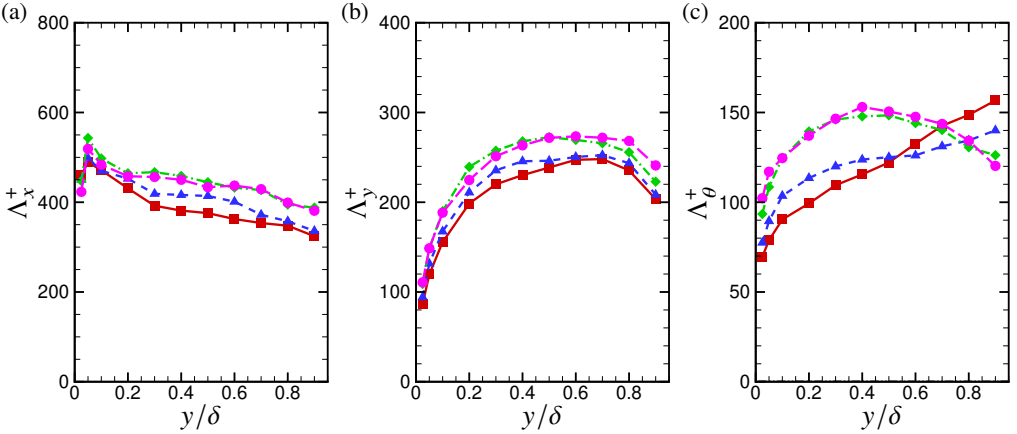


Figure 28: Inner-scaled integral lengths in (a) streamwise, (b) wall-normal, and (c) azimuthal directions as a function of y at four streamwise locations: — with \blacksquare , $x/D = 0.21$; - - - with \blacktriangle , $x/D = 0.43$; - · - · with \blacklozenge , $x/D = 0.71$; - · - · with \bullet , $x/D = 0.99$.

APG axisymmetric TBL show a much weaker growth in y and reach peak values closer to the wall than that of the ZPG TBL. Note that the decline of the wall-normal correlation lengths near the boundary-layer edge is caused by capping the upper bound of the integral (4.4) at $y/\delta = 1$, rather than a true decrease in the physical length scale. For the azimuthal integral length, similar values across different streamwise locations are observed within the near-wall region. However, their wall-normal variations in the outer region show diverging trends for different streamwise locations. At $x/D = 0.21$, the integral length increases almost linearly away from the wall at a rate similar to that of the reference ZPG TBL. This rate of increase is much reduced at $x/D = 0.43$. Further downstream, at $x/D = 0.71$ and 0.99 , the integral lengths begin to decrease above a wall-normal distance of $y/\delta \approx 0.4$. This qualitatively different behavior is likely due to the increasing effect of transverse curvature towards the end of the tail cone.

In figure 28, the distributions of the integral lengths in wall units are depicted. A notable

observation is that their streamwise variations exhibit a trend opposite to that of their outer-scaled counterparts seen in figure 27. The inner-scaled integral lengths show a mild increase in the downstream direction except for the azimuthal integral length in the outer region of the boundary layer, where the opposite is noted.

5. Conclusion

In this study, large-eddy simulation has been employed to investigate the characteristics and structure of an axisymmetric TBL under strong APG. The TBL is on the tail cone of a BOR at zero angle of attack, as in the experimental setup described by Balantrapu *et al.* (2021, 2023). The BOR length is 3.17 times the diameter D , of which the last $1.17D$ is the tail cone that has a 20° half apex angle. The Reynolds number based on the free-stream velocity and the BOR length is 1.9×10^6 . To reduce the computational expense, an equilibrium wall model is employed in the nose and midsection of the BOR, while the tail-cone section is computed with wall-resolved LES. Detailed comparisons of velocity and wall-pressure statistics between the numerical and experimental results have verified the accuracy of the simulation, and demonstrated the efficacy of the zonal wall-modeled LES approach in accurately capturing the spatio-temporal characteristics of the nonequilibrium, axisymmetric TBL under the influences of APG and transverse curvature. The simulation data significantly enhances the experimental measurements documented by Balantrapu *et al.* (2021, 2023) for this fundamentally interesting flow, and provides new insights into the turbulence physics.

Utilizing flow-field data from the LES, the statistics of the nonequilibrium axisymmetric TBL on the tail cone and the evolution of turbulence structures are investigated in a region where the momentum-thickness Reynolds number varies from 3,420 to 12,600 and the friction Reynolds number varies from 955 to 1,650. The Clauser pressure-gradient parameter β based on the wall pressure increases progressively downstream from 4.61 to 11.2, whereas its value based on the pressure at the boundary-layer edge is within a much narrower range of 4.15 to 6.03 due to the increasing pressure variation across the decelerating boundary layer. The transverse curvature parameters δ/r_s and r_s^+ are within 0.12 to 0.94 and 1,760 to 8,260, respectively, indicating that the curvature effect is relatively small. The major findings of this investigation are:

- Similar to planar TBLs under APG (Harun *et al.* 2011), the inner-scaled mean streamwise velocity profiles of the axisymmetric TBL exhibit a distinguishable logarithmic region. However, this region is characterized by a shorter range and a slightly steeper slope than the classical logarithmic law. As the APG grows downstream, the profiles fall below the standard logarithmic law, leading to a more pronounced wake region.
- With the embedded-shear-layer scaling (Schatzman & Thomas 2017), the mean streamwise velocity profiles demonstrate very good self-similarity over a wide range of wall-normal distance, confirming the scaling results of Balantrapu *et al.* (2021). The three components of turbulence intensity also exhibit a reasonable degree of self-similarity. However, the application of embedded-shear-layer scaling to Reynolds shear stress is more restrictive and only valid in a smaller portion of the outer region.
- The pre-multiplied azimuthal-wavenumber spectra of streamwise velocity fluctuations have two distinct peaks along the wall-normal coordinate. The inner peak, located at $y^+ \approx 12$, is characterized by a mean azimuthal wavelength of approximately 100 wall units. This wavelength, indicative of the average spacing between near-wall elongated streaks, is similar to that in ZPG planar TBLs but shows a slight decrease in the downstream direction as the intensity of the peak decays significantly. The outer peak, positioned in the wake region, increases in strength, wavelength and distance from the wall in the downstream direction as

increasingly larger-scale motions are energized. The azimuthal wavelength of the peak is less than one half of the corresponding spanwise wavelength in a ZPG TBL.

- Large-scale turbulence structures based on the two-point correlations of streamwise velocity fluctuations show rapid growth and elongation in the thickening axisymmetric TBL. However, relative to the local boundary-layer thickness, the structures decrease in size toward downstream, accompanied by increasing inclination angles that are significantly larger than typical values in plane channel flows and ZPG TBLs.

- The integral lengths in all three directions relative to δ are qualitatively similar to, but substantially smaller than those in ZPG planar TBLs at comparable Reynolds numbers. While the streamwise integral length decreases with the wall-normal distance in the outer layer, the wall-normal and azimuthal integral lengths increase with the wall-normal distance except at downstream stations, where the trend is reversed in the outer region for the azimuthal length.

Acknowledgments

This research was supported by the Office of Naval Research under grants N00014-17-1-2493 and N00014-20-1-2688, with Drs. Ki-Han Kim and Yin Lu Young as Program Officers. Computer time was provided by the U.S. Department of Defense High Performance Computing Modernization Program (HPCMP) and Center for Research Computing (CRC) at the University of Notre Dame. The authors gratefully acknowledge Drs. William Devenport, Nathan Alexander and N. Agastya Balantrapu for providing experimental data and helpful discussions. D.Z. is grateful to Dr. Xinyue E. Zhao for her help with data post-processing. A Portion of this work in a preliminary form was presented in AIAA Paper 2020-2989, AIAA Aviation 2020 forum (online).

Declaration of Interests

The authors report no conflict of interest.

REFERENCES

- AUBERTINE, C. D. & EATON, J. K. 2005 Turbulence development in a non-equilibrium turbulent boundary layer with mild adverse pressure gradient. *J. Fluid Mech.* **532**, 345–364.
- AUBERTINE, C. D. & EATON, J. K. 2006 Reynolds number scaling in a non-equilibrium turbulent boundary layer with mild adverse pressure gradient. *Int. J. Heat Fluid Flow* **27**, 566–575.
- BALANTRAPU, N. A., ALEXANDER, W. N. & DEVENPORT, W. 2023 Wall-pressure fluctuations in an axisymmetric boundary layer under strong adverse pressure gradient. *J. Fluid Mech.* **960**, A28.
- BALANTRAPU, N. A., HICKLING, C., ALEXANDER, W. N. & DEVENPORT, W. 2021 The structure of a highly decelerated axisymmetric turbulent boundary layer. *J. Fluid Mech.* **929**, A9.
- CABOT, W. & MOIN, P. 2000 Approximate wall boundary conditions in the large-eddy simulation of high Reynolds number flow. *Flow Turbul. Combust.* **63**, 269–291.
- CHEN, P., WU, W., GRIFFIN, K. P., SHI, Y. & YANG, X. 2023 A universal velocity transformation for boundary layers with pressure gradients. *J. Fluid Mech.* **970**, A3.
- CHRISTENSEN, K. T. & WU, Y. 2005 Characteristics of vortex organization in the outer layer of wall turbulence. In *Proceedings of the Fourth International Symposium on Turbulence and Shear Flow Phenomena, Williamsburg, Virginia*.
- CLAUSER, F. H. 1954 Turbulent boundary layers in adverse pressure gradients. *J. Aeronaut. Sci.* **21**, 91–108.
- COLES, D. 1956 The law of the wake in the turbulent boundary layer. *J. Fluid Mech.* **1**, 191–226.
- FUJINO, S. & SEKIMOTO, T. 2012 Performance evaluation of GP-BiCGSafe method without reverse-ordered recurrence for realistic problems. In *Proceedings of the International MultiConference of Engineers and Computer Scientists 2012*, vol. II, pp. 1673–1677. International Association of Engineers.
- GERMANO, M., PIOMELLI, U., MOIN, P. & CABOT, W. H. 1991 A dynamic subgrid-scale eddy viscosity model. *Phys. Fluids A* **3**, 1760–1765.

- GROVES, N. C., HUANG, T. T. & CHANG, M. S. 1989 Geometric characteristics of DARPA (Defense Advanced Research Projects Agency) SUBOFF models (DTRC model numbers 5470 and 5471). *Tech. Rep.* David Taylor Research Center, Bethesda, MD.
- GUNGOR, T. R., MACIEL, Y. & GUNGOR, A. G. 2024 Turbulent activity in the near-wall region of adverse pressure gradient turbulent boundary layers. *J. Phys. Conf. Ser.* **2753**, 012005.
- HAMMACHE, M., BROWAND, F. K. & BLACKWELDER, R. F. 2002 Whole-field velocity measurements around an axisymmetric body with a stratford-smith pressure recovery. *J. Fluid Mech.* **461**, 1–24.
- HARUN, Z., MONTY, J. & MARUSIC, I. 2011 The structure of zero, favorable, and adverse pressure gradient turbulent boundary layers. In *Proceedings of the 7th International Symposium on Turbulence and Shear Flow Phenomena, Ottawa, Canada*.
- HARUN, Z., MONTY, J. P., MATHIS, R. & MARUSIC, I. 2013 Pressure gradient effects on the large-scale structure of turbulent boundary layers. *J. Fluid Mech.* **715**, 477–498.
- HICKLING, C., BALANTRAPU, N. A., ALEXANDER, W. N., MILLICAN, A. J., DEVENPORT, W. J. & GLEGG, S. A. 2019 Turbulence ingestion into a rotor at the rear of an axisymmetric body. *AIAA Paper* 2019-2571 .
- HUANG, T. T., LIU, H. L., GROVES, N. C., FORLINI, T. J., BLANTON, J. N. & GOWING, S. 1992 Measurements of flows over an axisymmetric body with various appendages in a wind tunnel: the DARPA SUBOFF experimental program. In *Proceedings of 19th Symposium on Naval Hydrodynamics, Seoul, Republic of Korea*. National Academy Press.
- JIMÉNEZ, J. 2018 Coherent structures in wall-bounded turbulence. *J. Fluid Mech.* **842**, P1.
- KROGSTAD, P.-Å. & SKÅRE, P. E. 1995 Influence of a strong adverse pressure gradient on the turbulent structure in a boundary layer. *Phys. Fluids* **7**, 2014–2024.
- KUMAR, P. & MAHESH, K. 2018 Large-eddy simulation of flow over an axisymmetric body of revolution. *J. Fluid Mech.* **853**, 537–563.
- LEE, J. H. 2017 Large-scale motions in turbulent boundary layers subjected to adverse pressure gradients. *J. Fluid Mech.* **810**, 323–361.
- LEE, J. H. & SUNG, H. J. 2009 Structures in turbulent boundary layers subjected to adverse pressure gradients. *J. Fluid Mech.* **639**, 101–131.
- LILLY, D. K. 1992 A proposed modification of the Germano subgrid-scale closure method. *Phys. Fluids A* **4**, 633–635.
- MACIEL, Y., SIMENS, M. P. & GUNGOR, A. G. 2017 Coherent structures in a non-equilibrium large-velocity-defect turbulent boundary layer. *Flow Turbul. Combust.* **98**, 1–20.
- MACIEL, Y., WEI, T., GUNGOR, A. G. & SIMENS, M. P. 2018 Outer scales and parameters of adverse-pressure-gradient turbulent boundary layers. *J. Fluid Mech.* **844**, 5–35.
- MARUSIC, I., MCKEON, B. J., MONKEWITZ, P. A., NAGIB, H. M., SMITS, A. J. & SREENIVASAN, K. R. 2010 Wall-bounded turbulent flows at high Reynolds numbers: recent advances and key issues. *Phys. Fluids* **22**, 065103.
- MARUSIC, I. & PERRY, A.E. 1995 A wall-wake model for the turbulence structure of boundary layers. part 2. further experimental support. *J. Fluid Mech.* **298**, 389–407.
- MATHIS, R., HUTCHINS, N. & MARUSIC, I. 2009 Large-scale amplitude modulation of the small-scale structures in turbulent boundary layers. *J. Fluid Mech.* **628**, 311–337.
- MONTY, J. P., HARUN, Z. & MARUSIC, I. 2011 A parametric study of adverse pressure gradient turbulent boundary layers. *Int. J. Heat Fluid Flow* **32**, 575–585.
- NAGANO, Y., TSUJI, T. & HOURA, T. 1998 Structure of turbulent boundary layer subjected to adverse pressure gradient. *Int. J. Heat Fluid Flow* **19**, 563–572.
- PATEL, V. C., NAKAYAMA, A. & DAMIAN, R. 1974 Measurements in the thick axisymmetric turbulent boundary layer near the tail of a body of revolution. *J. Fluid Mech.* **63**, 345–367.
- PIQUET, J. & PATEL, V. C. 1999 Transverse curvature effects in turbulent boundary layer. *Prog. Aerosp. Sci.* **35**, 661–672.
- POSA, A. & BALARAS, E. 2016 A numerical investigation of the wake of an axisymmetric body with appendages. *J. Fluid Mech.* **792**, 470–498.
- POSA, A. & BALARAS, E. 2020 A numerical investigation about the effects of Reynolds number on the flow around an appended axisymmetric body of revolution. *J. Fluid Mech.* **884**, A41.
- SCHATZMAN, D. M. & THOMAS, F. O. 2017 An experimental investigation of an unsteady adverse pressure gradient turbulent boundary layer: embedded shear layer scaling. *J. Fluid Mech.* **815**, 592–642.
- SILLERO, J. A., JIMÉNEZ, J. & MOSER, R. D. 2014 Two-point statistics for turbulent boundary layers and channels at Reynolds numbers up to $\delta^+ \approx 2000$. *Phys. Fluids* **26**, 105109.

- SMITS, A. J., MCKEON, B. J. & MARUSIC, I. 2011 High-Reynolds number wall turbulence. *Annu. Rev. Fluid Mech.* **43**, 353–375.
- SPALART, P.R. & WATMUFF, J.H. 1993 Experimental and numerical study of a turbulent boundary layer with pressure gradients. *J. Fluid Mech.* **249**, 337–371.
- STRATFORD, B. S. 1959 An experimental flow with zero skin friction throughout its region of pressure rise. *J. Fluid Mech.* **5**, 17–35.
- VOLINO, R. J. 2020 Non-equilibrium development in turbulent boundary layers with changing pressure gradients. *J. Fluid Mech.* **897**, A2.
- WANG, H., WANG, S. & HE, G. 2018 The spanwise spectra in wall-bounded turbulence. *Acta Mech. Sinica* **34**, 452–461.
- WANG, M. & MOIN, P. 2002 Dynamic wall modeling for large-eddy simulation of complex turbulent flows. *Phys. Fluids* **14**, 2043–2051.
- WEI, T. & KNOPP, T. 2023 Outer scaling of the mean momentum equation for turbulent boundary layers under adverse pressure gradient. *J. Fluid Mech.* **958**, A9.
- YOU, D., HAM, F. & MOIN, P. 2008 Discrete conservation principles in large-eddy simulation with application to separation control over an airfoil. *Phys. Fluids* **20**, 101515.
- ZAGAROLA, M. V. & SMITS, A. J. 1998 Mean-flow scaling of turbulent pipe flow. *J. Fluid Mech.* **373**, 33–79.
- ZHOU, D., WANG, K. & WANG, M. 2020 Large-eddy simulation of an axisymmetric boundary layer on a body of revolution. *AIAA Paper* 2020-2989 .
- ZHOU, D., WANG, K. & WANG, M. 2024 Rotor aeroacoustic response to an axisymmetric turbulent boundary layer. *J. Fluid Mech.* **981**, A25.